HI Intensity Mapping on GMRT Observations with the Tapered Gridded Estimator

Satyapan Munshi

A dissertation submitted for the partial fulfilment of

BS-MS Dual Degree in Science

Indian Institute of Science Education and Research Mohali

April 2021

Certificate of Examination

This is to certify that the dissertation titled "**HI Intensity Mapping on GMRT Observations with the Tapered Gridded Estimator**" submitted by **Mr. Satyapan Munshi (Reg. No. MS16099)** for the partial fulfilment of BS-MS Dual Degree programme of the Institute, has been examined by the thesis committee duly appointed by the Institute. The committee finds the work done by the candidate satisfactory and recommends that the report be accepted.

Dr. A. Joseph Dr. H. K. Jassal Prof. K. P. Singh Prof. J. S. Bagla
(Supervisor)

Dated: April 29, 2021

Declaration

The work presented in this dissertation has been carried out by me under the guidance of Prof. Jasjeet Singh Bagla at the Indian Institute of Science Education and Research, Mohali.

This work has not been submitted in part or in full for a degree, a diploma, or a fellowship to any other university or institute. Whenever contributions of others are involved, every effort is made to indicate this clearly, with due acknowledgement of collaborative research and discussions. This thesis is a bonafide record of original work done by me and all sources listed within have been detailed in the bibliography.

Satyapan Munshi
(Candidate)

Dated: April 29, 2021

In my capacity as the supervisor of the candidate's project work, I certify that the above statements by the candidate are true to the best of my knowledge.

Prof. Jasjeet Singh Bagla
(Supervisor)

Acknowledgements

I will begin by thanking my supervisor Jasjeet Singh Bagla for allowing me to work with him on this as well as on several other interesting projects during my stay at IISER. He introduced me to this fascinating field of radio astronomy and has been a source of constant support and encouragement in my academic endeavours throughout my undergraduate studies.

I am grateful to Somnath Bharadwaj, Asif Elahi, Samir Choudhuri and Srijita Pal, who have provided me with the programs for the TGE which was applied to the final dataset. I want to thank Pranav Kukreti, who reduced the GMRT software backend raw dataset and Apurba Bera who reduced the GMRT wideband backend dataset which were used in this analysis. I also thank Nissim Kanekar and Jayaram Chengalur, for their help during the project.

Over my undergraduate years, I have met some wonderful people who have had a lasting impact on me, both academically and personally. I would like to thank Avinash Deshpande for inspiring me to pursue interesting projects with the SWAN telescope and for always being open to discussions related to astrophysics. The frequent discussions on radio astronomy with Pavan and on various topics in physics with Sarbojoy, Vikram Da, Saurav have played a big part in my learning experience. I want to thank Ishan Da for the numerous memorable experiences we have had during our musical performances together and Subhajit and Upayan for the early morning tennis matches which were a source of relaxation to regularly look forward to. My stay at Mohali would not have been the same without my friends and I thank all of them for the unforgettable 5 years we have spent together.

The acknowledgements would be incomplete without mentioning my family, who have always encouraged me to pursue my interests and have been there for me in times of difficulty. It is impossible to thank my mother enough, for her contribution towards my well being.

List of Figures

Contents

Abstract

One of the foremost challenges in modern astrophysics and cosmology is to get observational constraints on theories of galaxy formation and evolution in a wide redshift range, ranging from the dark ages to the present epoch. Observing the redshifted 21 cm signal of neutral hydrogen (HI) allows us to probe the large scale structure in these epochs using radio telescopes. In the post reionization era, the HI is expected to be confined in the dense interiors of galaxies and hence, the spatial distribution of HI should trace the galaxy distribution and, in turn, the dark matter distribution. HI Intensity Mapping is a novel technique which uses low angular resolution observations using radio interferometers to measure the 3 dimensional distribution of integrated HI emission from a large number of galaxies. This allows us to build up the signal to noise by averaging the signal in large comoving volumes and get a statistical estimate of the large scale structure distribution.

In this project, we perform HI intensity mapping with the upgraded Giant Metrewave Radio Telescope. For this purpose, we use the Tapered Gridded Estimator [Choudhuri 14] which is a visibility based estimator for the HI power spectrum. In the first part of the project, we use simulations of GMRT observations to implement the estimator and then test its performance in different situations. We see that the estimator is able to recover the input power spectrum from the simulated data at all but the very large scales, possibly because of the lack of very small baselines in the GMRT antenna distribution. Next, the estimator is applied to actual observations of the Extended Groth Strip made using the GMRT at a redshift of 0.028. All point sources above a threshold of 7σ are modelled and subtracted. The Multifrequency Angular Power Spectrum ($C_\ell(\Delta\nu)$), the cylindrical power spectrum $P(k_\perp, k_\parallel)$ and the spherical power spectrum ($P(k)$) are measured using the TGE and the effect of point source subtraction and tapering on these quantities is studied. Both tapering and point source subtraction are seen to have a significant effect in the suppression of foregrounds. We employ a foreground avoidance technique to average the power values in a region outside the foreground wedge in spherical k shells to estimate the spherical power spectrum, which is then used to set the upper limits on the dimensionless HI power spectrum ($\Delta^2(k)$) at z = 0.028 and in the relevant wave modes. The dark matter power spectrum at z = 0.028 is calculated and used to get upper limits on the quantity $\Omega_{HI} \times b_{HI}$. We obtain the tightest constraints at k = 20.73 Mpc^{-1} and the estimated 2σ upper limits at this mode are $\Delta^2(k) = (17.14)^2 mK^2$ and $\Omega_{HI} b_{HI} = 0.0179$. A similar analysis is then done on EGS observations with the GMRT at z=0.34 and z=0.38. The tightest constraints from this analysis are: $\Delta^2_U(k) = (54.28)^2 mK^2$ and $\Omega_{HI} b_{HI} = 6.02 \times 10^{-2}$ at k=5.56Mpc^{-1} (for z=0.34) and $\Delta^2_U(k) = (71.32)^2 mK^2$ and $\Omega_{HI} b_{HI} = 8.61 \times 10^{-2}$ at k=3.60Mpc^{-1} (for z=0.38).

Chapter 1

Introduction

Over the last few centuries, we have made tremendous progress in answering some of the fundamental questions related to the evolution of the universe and the structures within it. It was not until the 20th century, however, that scientists started to create quantitative models of the evolution of the universe, when Einstein proposed his General Theory of Relativity. The Big Bang Model of the universe was born and soon we had a relatively well established theoretical picture of the evolution of the universe and the celestial bodies within it. But it was very difficult to test these theories through observations, particularly since we were confined primarily to the visible wavelengths of light. Throughout the last century, the advancement in technology has allowed us to expand our window to a much wider part of the electromagnetic spectrum and we have utilized this to probe the various mysteries of the universe.

Radio astronomy was born in the 1930s, when Karl Jansky pointed his rotating antenna towards the night sky and detected static emission at 20 MHz that repeated every sidereal day [Jansky 33]. The technology of radar received a huge boost during the operations of the Second World War and since then, scientists have been building bigger and more sensitive telescopes to observe the sky in radio wavelengths. The main advantage of observing in radio frequencies is that radio waves are practically unaffected by the atmosphere in a wide frequency range. This permits us to construct telescopes on the ground without worrying about losing out on information due to scattering in the Earth's atmosphere. The major drawback of radio astronomy, however, is that the diffraction limit of a telescope ($\theta \approx \lambda/d$ where λ is the wavelength and d is the diameter of aperture) at radio wavelengths is very large. This prevents us from achieving reasonably good angular resolution without building telescopes of humongous sizes. This issue was circumvented in the 1940s with the emergence of ra-

dio interferometry, a technique which combines signals from separate antennas placed at large distances to mimic a telescope of huge diameter. A brief description of the method of radio interferometry has been presented in 2.1.

Ever since its advent, radio astronomy has been used to study the universe and has resulted in some of the most important discoveries in astrophysics and cosmology. In 1951, Ewen and Purcell detected a spectral line emission from the Milky Way at a wavelength of 21 cm [Ewen 51]. The discovery of the Cosmic Microwave Background Radiation (CMBR), a relic signal from the infancy of the universe, was made by Penzias and Wilson in 1964 using their 6m horn antenna [Penzias 65]. The study of the CMBR has revolutionized our understanding of cosmology and is the most important observational evidence of the validity of the Big Bang Theory. Galaxy surveys in the optical have given us a huge wealth of information till the time when the universe was about a billion years old. However, in spite of these efforts, a large part of the history of the universe is unexplored. This is precisely where 21 cm cosmology comes in. It gives us the opportunity to probe very large volumes of the universe by mapping the redshifted 21 cm signal. The remainder of this chapter gives an introduction to the field of 21 cm cosmology. Many of the concepts presented here are described in much more detail in the review by Liu and Shaw [Liu 20] and the interested reader is suggested to consult the same.

1.1 Physics of the 21 cm Signal

The 21 cm signal arises from the hyperfine transition of neutral hydrogen (HI). The interaction of the electron and the nuclear magnetic dipole moments splits the ground state of HI into two hyperfine split states with F=1 and F=0, depending on the relative alignment of the nuclear and electron spins. Here $\boldsymbol{F} = \boldsymbol{S}+\boldsymbol{I}$ = total angular momentum, $\boldsymbol{S}$ = electron spin angular momentum, $\boldsymbol{I}$ = nuclear spin angular momentum. The upper F=1 state is three fold degenerate and is called the triplet state while the lower F=0 state is called the singlet state. The energy difference between the triplet and the singlet states corresponds to a frequency of 1420.4 MHz or a wavelength of 21 cm. Figure 1.1 shows the energy level diagram for the ground state of HI.

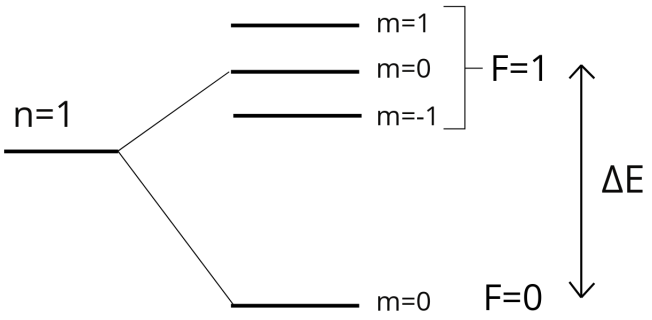

Figure 1.1: Energy level diagram showing the hyperfine splitting of the ground state (n=1) of neutral hydrogen.

1.1.1 Spin Temperature

In order to quantify the ratio of the population of HI in the two hyperfine split states, a quantity called the spin temperature (T_S) is used. The spin temperature is defined as:

$$\frac{n_1}{n_0} = 3 \times e^{-T_*/T_S} \tag{1.1}$$

where n_1 and n_0 are the population of HI atoms in the higher and lower hyperfine states respectively, T_* equals $\frac{h\nu_*}{k_B}$ ($\nu_* = 1420.4$ MHz) and the factor of 3 accounts for the three fold degeneracy of the triplet state.

There are three processes which are primarily responsible for deciding the ratio of the population of HI in the upper and lower hyperfine states:

Radiative Transition: External radiation (CMBR) can cause excitation or de-excitation through stimulated emission or absorption. If the gas is in equilibrium with this radiation, the spin temperature approaches the temperature of the radiation field (T_γ).

Collisional Transition: Collisions between HI atoms or between HI atoms and electrons can lead to a spin flip. If the transition comes to equilibrium with the collisions, then this drives the T_S towards the kinetic temperature (T_K).

Wouthuysen Field Effect: Absorption of a Lyman alpha photon from UV radiation can lead to a transition from the n=1 to the n=2 state. When the atom comes back to the ground state, if it returns to a different hyperfine state than before, a spin flip has occurred. This is called the Wouthuysen Field Effect. In equilibrium, this effect tries to bring the spin temperature towards the color temperature (T_C) which describes the slope of the radiation field around the Lyman alpha line.

1.1.2 Brightness Temperature Fluctuations

Observationally, the quantity of interest for us is the contrast between T_γ and T_S and this decides whether the signal is seen in absorption or emission. The brightness temperature of the 21 cm line is given by:

$$\delta T_b(\hat{\boldsymbol{n}}, \nu) = \frac{T_S - T_\gamma}{1+z}\left(1 - e^{-\tau(\hat{\boldsymbol{n}},\nu)}\right) \tag{1.2}$$

Here z is the redshift and $\tau(\hat{\boldsymbol{n}}, \nu)$ is the optical depth along the line of sight direction $\hat{\boldsymbol{n}}$ at an observation frequency of ν ($= \frac{\nu_*}{1+z}$). It can be shown that $\tau(\hat{\boldsymbol{n}}, \nu)$ is given by (Appendix of [Bharadwaj 05]):

$$\tau(\hat{\boldsymbol{n}}, \nu) = \frac{3c^2 A_{10} n_{HI} T_*}{32\pi\nu_*^3 H(a) T_S}\left(1 - \frac{1}{aH(a)}\frac{\partial v}{\partial r}\right) \tag{1.3}$$

where A_{10} is the spontaneous emission coefficient of the 21 cm line, n_{HI} is the number density of HI atoms, a=$\frac{1}{1+z}$ is the scale factor, H(a) is the Hubble parameter and $\frac{\partial v}{\partial r}$ is the line of sight derivative of the radial component of the peculiar velocity. Since the HI 21 cm line is typically optically thin in galaxies, we can make the approximation $\tau(\hat{\boldsymbol{n}}, z) \ll 1$ and Taylor expand equation 1.2. Then putting in the expression of $\tau(\hat{\boldsymbol{n}}, z)$ and simplifying, we get [Bharadwaj 05]:

$$\delta T_b(\hat{\boldsymbol{n}}, \nu) = \left(1 - \frac{T_\gamma}{T_S}\right)\bar{T}(z)\frac{\rho_{HI}}{\bar{\rho}_H}\left(1 - \frac{1+z}{H(z)} \times \frac{\partial v}{\partial r}\right) \tag{1.4}$$

where $\bar{T}(z) \approx (4.0 \text{ mK}) \times (1+z)^2 \left(\frac{\Omega_b h^2}{0.02}\right)\left(\frac{0.7}{h}\right)\left(\frac{H_0}{H_z}\right)$ depends only on the cosmological parameters and $\frac{\rho_{HI}}{\bar{\rho}_H}$ is the ratio of neutral hydrogen density to the mean hydrogen density. If we neglect peculiar velocities, this reduces to:

$$\delta T_b(\hat{\boldsymbol{n}}, \nu) = \left(1 - \frac{T_\gamma}{T_S}\right)\bar{T}(z)\bar{x}_{HI} \tag{1.5}$$

where $\bar{x}_{HI} = \frac{\rho_{HI}}{\bar{\rho}_H}$ is the mean neutral hydrogen fraction. So the neutral fraction and the difference between the spin temperature and CMBR temperature are the two key parameters which guide the observed brightness temperature fluctuations.

1.1.3 Power Spectrum

If we want to gain a theoretical understanding of the brightness temperature fluctuations of the 21 cm radiation, the quantities we define should correspond to the statistical process guiding the fluctuations and not the realization of that process, i.e., the fluctuations themselves. The quantity which is commonly used to do this is the power spectrum. The power spectrum is defined as the scale dependent variance of the brightness temperature fluctuations in the spatial frequency space. Assuming that the fluctuations follow a Gaussian distribution, the power spectrum completely specifies the statistics of the underlying process generating the fluctuations. The HI power spectrum $P_{HI}(\boldsymbol{k})$ is defined as:

$$\left\langle \Delta T_b(\boldsymbol{k}) \Delta T_b^*(\boldsymbol{k'}) \right\rangle = (2\pi)^3 \delta^3(\boldsymbol{k} - \boldsymbol{k'}) P_{HI}(\boldsymbol{k}) \tag{1.6}$$

where $\langle \cdots \rangle$ denotes an ensemble average over multiple realizations of the Gaussian random field and $\Delta T_b(\boldsymbol{k})$ is the Fourier transform of $\delta T_b(\boldsymbol{r})$ and is given by:

$$\delta T_b(\boldsymbol{r}) = \int \frac{d^3k}{(2\pi)^3} e^{i\boldsymbol{k}\cdot\boldsymbol{r}} \Delta T_b(\boldsymbol{k}) \tag{1.7}$$

Combining equations 1.4, 1.6 and 1.7, we arrive at the following expression relating the 21 cm power spectrum with the matter power spectrum [Bharadwaj 05]

$$P_{HI}(\boldsymbol{k}) = (\bar{T}\bar{x}_{HI} b_{HI})^2 (1 + \beta\mu^2)^2 P(k) \tag{1.8}$$

where $\beta \approx \frac{\Omega_m^{0.6}}{b_{HI}}$ with Ω_m being the mass density of non relativistic matter as a fraction of the critical mass density and $\mu = \hat{\boldsymbol{k}} \cdot \hat{\boldsymbol{n}}$. In obtaining this equation, it has been assumed that the HI clouds are biased with respect to the dark matter distribution by a linear bias (bias factor: b_{HI}), $T_S \gg T_\gamma$ in the post reionization universe and that the distribution of matter in the scales of interest is isotropic.

Another way to describe the second order statistics of the brightness temperature fluctuations, which can be more convenient for radio interferometric observations, is

the Multi-frequency Angular Power Spectrum or MAPS [Datta 07]. In order to define it, the brightness temperature fluctuations are decomposed in the basis of spherical harmonics $Y_\ell^m(\hat{\boldsymbol{n}})$ as:

$$\delta T_b(\hat{\boldsymbol{n}}, \nu) = \sum_{\ell,m} a_{\ell m}(\nu) Y_\ell^m(\hat{\boldsymbol{n}}) \tag{1.9}$$

The MAPS is then defined as:

$$\left\langle \Delta T_b(\boldsymbol{k}_\perp, \nu_a) \Delta T_b^*(\boldsymbol{k}'_\perp, \nu_b) \right\rangle = C_{k_\perp}(\nu_a, \nu_b) \delta^2(\boldsymbol{k}_\perp - \boldsymbol{k}'_\perp) \tag{1.10}$$

Here $\boldsymbol{k}$ has been replaced by $(\boldsymbol{k}_\perp, \nu)$ as the projection of the wave vector in the plane of the sky, as a function of frequency. From Equations 1.9 and 1.10, and using $k_\perp = \ell/r$ (where r is the comoving distance at the central observing frequency ν_c), we finally obtain:

$$C_\ell(\nu_a, \nu_b) = \frac{1}{2\ell + 1} \sum_{m=-\ell}^{\ell} a_{\ell m}(\nu_a) a^*_{\ell m}(\nu_b) \tag{1.11}$$

Under the assumption that the redshifted 21 cm signal is statistically homogeneous along the frequency axis, $C_\ell(\nu_a, \nu_b) = C_\ell(\Delta\nu)$ with $\Delta\nu = |\nu_a - \nu_b|$. In the flat sky approximation, the cylindrical power spectrum is related to the $C_\ell(\Delta\nu)$ via the following expression [Datta 07]:

$$P(k_\perp, k_\parallel) = r^2 r' \int_{-\infty}^{\infty} d(\Delta\nu) e^{-ik_\parallel r' \Delta\nu} C_\ell(\Delta\nu) \tag{1.12}$$

where $r' = \frac{dr}{d\nu}\Big|_{\nu=\nu_c}$ is the rate of change of r with frequency, evaluated at ν_c and $k_\parallel$ is the projections of $\boldsymbol{k}$ along the line of sight.

1.2 Evolution of the Global Signal

In Equation 1.5, we see that the brightness temperature of HI is linked to the neutral hydrogen fraction and the contrast between the spin temperature and the temperature of the background radiation (which is assumed to be the CMBR). Our present understanding of the evolution of the universe results in predictions about the magnitude of the global 21 cm signal at different redshifts. Following is a brief summary of the different epochs and how the global signal is expected to behave in each of these redshift ranges.

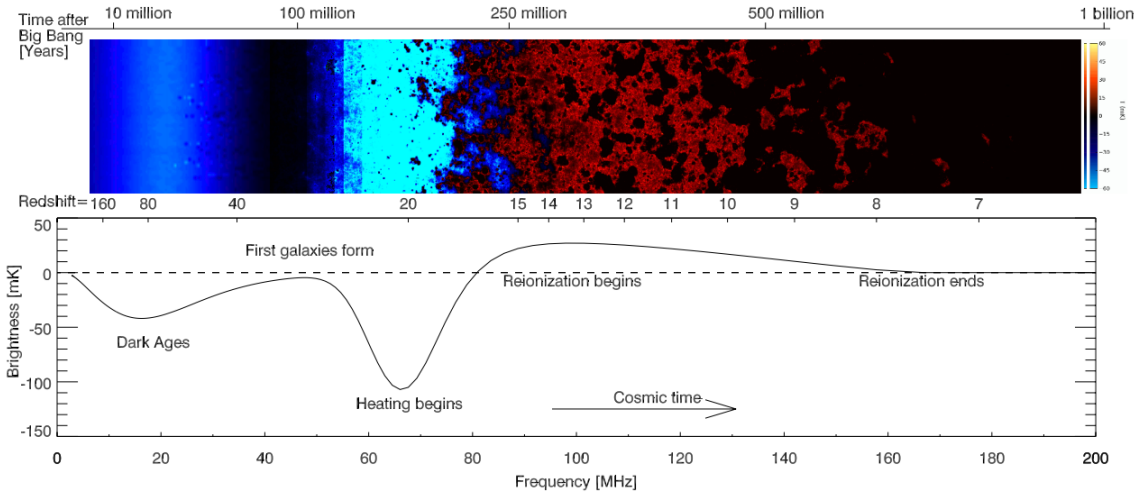

Figure 1.2: Top: 2d slice of the 21 cm brightness temperature distribution. Bottom: The global 21 cm signal. Source: [Pritchard 12].

The Dark Ages ($25 < z < 1100$)**:** Around z = 1100, the universe undergoes recombination, when it has cooled sufficiently to allow the recombination of protons and electrons to form neutral hydrogen. The photons, which till then had a very small mean free path due to the large Thompson scattering cross section of electrons, are now free to move across the universe and these photons form the CMBR. After recombination, the CMBR photons undergo inverse Compton scattering with the residual electrons and this couples the gas temperature T_K to the CMBR temperature T_γ. The T_S is in turn coupled to T_K and hence there is no signal till z = 200 when the scatterings become rare. Now T_K falls as $\frac{1}{(1+z)^2}$ while T_γ falls as $\frac{1}{1+z}$. Since T_S is coupled to T_K, δT_b falls and the 21 cm signal is seen in absorption against the CMBR. Around z = 50, the gas has cooled to an extent that collisional coupling is no longer effective. The T_S is then driven towards the T_γ and δT_b starts rising. Around z = 30, $T_S \approx T_\gamma$ and δT_b becomes 0. This period ($25 < z < 1100$) is referred to as the Dark Ages since there is no source of radiation other than the CMB and the fluctuations in the $\delta T_b(\hat{\boldsymbol{n}})$ are sourced by the density fluctuations.

Cosmic Dawn and Epoch of Reionization ($6 < z < 25$) The first luminous objects are formed around z = 25 and these sources produce an abundance of Lyman α photons. These photons are in equilibrium with the gas ($T_C \approx T_K$) and through the Wouthuysen Field Effect, T_S is driven towards T_K. Since $T_K < T_\gamma$, $\delta T_b < 0$ and the signal is again seen in absorption. Once the heating due to X-ray photons emitted

by the luminous sources becomes significant, T_K increases. T_S which is coupled to T_K follows it so that at some point, $T_S = T_K = T_\gamma$ and $\delta T_b = 0$. After this, the heating continues and $T_S = T_K > T_\gamma$ meaning that the signal is now seen in emission. Throughout this epoch, the radiation from the sources ionizes the HI around the sources, resulting in bubbles around the sources containing ionized Hydrogen (HII) which give no 21 cm signal. These bubbles grow in size, eventually merging with each other and the universe becomes completely ionized. This completes the epoch of reionization, a period of extremely rich astrophysics and one of the most important periods in the expansion history of the universe.

Post Reionization ($z < 6$) After reionization is complete, the HI is confined to dense pockets in the interiors of galaxies where they can be effectively shielded from the ionizing radiation. Any remaining 21 cm signal arises primarily from these galaxies. Observations in this redshift range are an excellent probe of cosmology, since the HI distribution directly traces the matter distribution. In addition to galaxy redshift surveys and measurements of Damped Lyman Alpha systems, a novel technique called Intensity Mapping offers a unique method to survey very large comoving volumes and estimate the Large Scale Structure distribution. One of the first targets of Intensity Mapping is to detect the Baryon Acoustic Oscillations, which are the remnants of primodial sound waves that are expected to leave an imprint of the matter power spectrum.

1.3 Foregrounds

The discussion in the previous sections has assumed that the intensity in the sky comes solely from the 21 cm signal. In practice however this is not true. In fact the sky at radio frequencies is dominated by radiation from other sources and these are referred to as foregrounds. The foregrounds can be upto 5 orders of magnitude higher than the actual 21 cm signal, which appears as a faint diffuse background. This poses serious challenges in the detection of the signal and has led to the emergence of a large number of techniques which attempt to isolate the signal from the bright foregrounds. According to their origin, foregrounds are classified into two main categories:

Galactic: The Galactic foregrounds consist primarily of the Diffuse Galactic Synchrotron Emission (DGSE). The synchrotron spectrum has a power law frequency dependence and the intensity becomes lower as we move to higher frequencies. There is a distinct spatial variation in the intensity of the DGSE and more emission is seen near the Galactic plane. The DGSE is partially linearly polarized. This polarized intensity is not necessarily a smooth function of frequency since differential Faraday Rotation in the interstellar medium can introduce complex frequency dependence. This can lead to complications in the mitigation of foregrounds, if the polarized intensity leaks into the total intensity due to inadequate calibration of the polarized response of the instrument. Apart from the DGSE, the free free emission from diffuse ionized gas and thermal dust also contributes to the Galactic foregrounds, but they become significant only at higher frequencies.

Extragalactic: The extragalactic foregrounds are mainly due to Active Galactic Nuclei (AGN) and Star Forming Galaxies (SFGs). The mechanism of emission in radio frequencies for both AGN and SFGs is primarily through synchrotron radiation. These sources appear as point sources in radio maps and need to be subtracted early in the data processing pipeline. However, faint point sources cannot be removed and the confusion caused by background fluctuations due to unresolved point sources can also contribute to foregrounds.

Chapter 2

HI Intensity Mapping

HI Intensity mapping, as the name suggests, is a technique by which the specific intensity of HI in the sky is mapped. If the 21 cm signal is the sole signal in the sky, then we can utilize the frequency bandwidth of the radio telescope to observe the signal at different redshifts by changing the observing frequency. Since different redshifts correspond to different radial distances in the sky, this allows us to build a 3d distribution of the HI Intensity in the sky. In the post reionization universe, which is the epoch are interested in, the HI is expected to be confined in the dense interiors of galaxies. Hence, mapping the HI distribution gives us an idea of the clustering of galaxies and in turn, the distribution of the underlying dark matter. In order to carry out HI intensity mapping to detect the redshifted 21 cm signal, we need to look at the sky in the radio wavelengths. But a single dish radio telescope suffers from the drawback that the angular resolution achievable by a telescope of diameter d is given by λ/d where λ is the observing wavelength. Hence achieving very good angular resolution requires the construction of telescopes of gigantic sizes. But as we increase the dish aperture, at some point, mechanical constraints come into play and it is not possible to construct steerable radio dishes with diameters beyond a certain limit. To get around this problem, astronomers use the technique of radio interferometry.

2.1 Radio Interferometry

In radio interferometry, the idea is to use a large number of receiving antennas at large distances from each other to mimic a radio telescope of huge diameter. Both the

amplitude and phase of the incoming electromagnetic wave are recorded by the antennas and the signals can later be added up in software. This is a cost effective method of reaching very high resolution using a set of smaller antennas. But the method demands high computational power and very precise calibration of the instrument in order to derive meaningful results.

2.1.1 Synthesis Imaging

Synthesis imaging is the method by which an array of radio antennas is used to produce an image of the sky. The simplest radio interferometer consists of two antennas separated by a distance. The vector connecting the two antennas of this two element interferometer is called the baseline vector. The signals received by the two antennas are time averaged and cross correlated in a correlator. The output of the correlator is called a "visibility". It can be shown that the visibility is one Fourier Component of the Intensity Distribution of the sky under the assumption that the sky signal is spatially incoherent and that the patch of the observed sky is small enough to be approximated as a 2d plane. The spatial frequency that the visibility samples is given by the projection of the baseline vector on the plane perpendicular to the source vector. The combination of a large number of antennas gives a large number of baseline vectors, and combined with the rotation of the earth, allows an effective sampling of the spatial frequency space. The components of the projected baseline vector, in the units of wavelength, are labelled by the letters u and v and hence the spatial frequency space is also called the uv space. The sky intensity distribution ($I_\nu(l,m)$) is a function of the direction cosines l and m, and is related to the visibilities (V(u,v)) through the Van Cittert-Zernike theorem:

$$V(u,v) = \int\int I_\nu(l,m) e^{-2\pi i(ul+vm)} dldm \tag{2.1}$$

This equation can potentially be inverted to obtain the sky intensity distribution. But the interferometer only has a finite set of baselines and a finite number of integrations during an observation. This results in an incomplete sampling of the spatial frequency space and this is quantified by the uv sampling function S(u,v). So the Fourier inverse of equation 2.1 yields the dirty image, not the true image. The dirty image ($I^D_\nu(l,m)$)

is given by:

$$I_\nu^D(l,m) = \int\int V(u,v)e^{2\pi i(ul+vm)}dudv \tag{2.2}$$

The dirty and true images are linked by a convolution:

$$I_\nu^D(l,m) = I_\nu(l,m) \circledast P(l,m) \tag{2.3}$$

Here P(l,m) is the Point Spread Function (PSF) and is the Fourier Transform of the uv sampling function S(u,v). Since we know the antenna distribution of an array and the observation parameters, we know S(u,v) and hence, P(l,m). $I_\nu^D(l,m)$ is obtained by Fourier transforming V(u,v). So, the problem essentially boils down to inverting equation 2.3 to obtain the true image $I_\nu(l,m)$. But this is a non trivial task and we need to make certain assumptions about the sky intensity distribution in order to get an estimate of the true image. The most common approach is to assume that the sky is made up of point sources and the algorithms which are used to iteratively deconvolve the true image from the dirty image are called the CLEAN algorithms.

2.1.2 Calibration

However, before the image is constructed from the visibilities, we need to make sure that the observed visibilities reflect the true visibilities and are not affected by the instrumental systematics. This crucial intermediate step is called calibration. Let V_{ij}^{obs} and V_{ij} be the observed and the ideal visibilities respectively, corresponding to the i^{th} and j^{th} antennas. Then the relation between them can be modelled as:

$$V_{ij}^{obs} = g_i g_j^* V_{ij} + n_{ij} \tag{2.4}$$

where g_i and g_j are complex gain factors and n_{ij} is the noise on the baseline. If the array has N number of antennas, then there are N(N-1)/2 ideal visibilities, N(N-1)/2 observed visibilities and N gain factors. So this is an underdetermined problem. But if we observe a field with a strong unresolved source, then we can make assumptions about the sky intensity distribution. This reduces the number of ideal visibilities to a small number, and we can simultaneously solve for them along with the N gain parameters using the N(N-1)/2 observed visibilities. Usually, this is done iteratively, and the calculated gain parameters can be then used to obtain the ideal visibilities

for the target field. Over the years, a set of reasonably well distributed, very bright radio sources have been identified as calibrators, and these are used for the purpose of calibration.

2.2 Visibility Correlations

Throughout 2.1, we had assumed that the antennas have a uniform response to different directions in the sky. This is not true in practice, and the antenna response is described by the primary beam $A(\boldsymbol{\theta})$. Hence the equation 2.1 gets modified to:

$$V(\boldsymbol{U},\nu) = \int d^2\theta e^{-2\pi i \boldsymbol{U}\cdot\boldsymbol{\theta}} A(\boldsymbol{\theta}) \delta I_\nu(\boldsymbol{\theta}) \tag{2.5}$$

Here, $\boldsymbol{\theta}$ is a vector in the plane of the sky with its origin at the phase centre of the observed field and $\boldsymbol{U}$ is the projected baseline vector in units of wavelength. The specific intensity from the redshifted HI emission has been decomposed into an isotropic component $\bar{I}_\nu$ and a fluctuating component $\delta I_\nu(\boldsymbol{\theta})$. The isotropic component is linked to the $\bar{T}(z)$ and only the fluctuating component contributes to the visibility. The intensity distribution in the sky is related to the brightness temperature fluctuations through the Rayleigh Jeans formula, which is a good approximation to Planck's law in radio frequencies:

$$\delta I_\nu(\boldsymbol{\theta}) = \frac{2k_B}{\lambda^2} \delta T_b(\boldsymbol{\theta},\nu) \tag{2.6}$$

The power spectrum is defined using equation 1.6, using cross correlations of brightness temperature fluctuations in the k space. The brightness temperature fluctuations are in turn linked to the visibilities using equation 2.5. Hence it is evident that, to obtain the power spectrum, we need to compute the cross correlations between visibilities. Combining equations 1.6, 1.7 and 2.5, we can obtain [Bharadwaj 05]:

$$\left\langle V(\boldsymbol{U},\nu) V^*(\boldsymbol{U}',\nu+\Delta\nu) \right\rangle = \bar{I}_\nu^2 \int \frac{d^3k}{(2\pi)^3} a(\boldsymbol{U} - \frac{r_\nu}{2\pi}\boldsymbol{k}_\perp) a^*(\boldsymbol{U'} - \frac{r_\nu}{2\pi}\boldsymbol{k}_\perp) P_{HI}(\boldsymbol{k}) e^{ik_\parallel r'_\nu \Delta\nu} \tag{2.7}$$

where $a(\boldsymbol{U})$ is the aperture power pattern and is the Fourier Transform of the primary beam $A(\boldsymbol{\theta})$.

2.3 The Tapered Gridded Estimator (TGE)

We saw in 2.2 that the visibility correlations can directly yield the power spectrum. Our choice of estimator for this project is the Tapered Gridded Estimator (TGE) [Choudhuri 14] [Choudhuri 16] [Bharadwaj 19] which is a visibility based estimator of the HI power spectrum.

2.3.1 Properties of the TGE

The TGE has the following main features:

Tapering The TGE tapers the sky response by convolving the visibilities with a window function. This is useful since the telescope primary beam is a complicated function of frequency, especially near the nulls and sidelobes. Hence, a point source lying in these regions can come in and out of the nulls and give rise to ripples in the power spectrum. These can be very difficult to model and hence this approach attempts to suppress the response of the telescope beyond a fraction of the distance to the first null of the primary beam.

Gridding The TGE evaluates the visibilities on a grid in the uv space and then works with them. This greatly reduces the computation time since there is no longer a need to cross correlate a large number of pairs of visibilities.

Subtraction of Noise Bias A very important issue in visibility correlations is that the correlation of a visibility with itself introduces a noise bias since this noise does not have a zero mean. The TGE internally models the noise bias and subtracts it to give an unbiased estimator of the MAPS (introduced in 1.1.3).

2.3.2 Constructing the TGE

To construct the TGE, the first step is to select a window function ($W(\boldsymbol{\theta})$) having a width equal to a fraction f (f < 1 for effective tapering) of the distance to the first null of the telescope primary beam. The window function is then Fourier transformed to

give $\tilde{\omega}(\boldsymbol{U}) = \mathcal{F}[\mathcal{W}(\boldsymbol{\theta})]$. Next, a grid in uv space is decided and the gridded convolved visibilities are evaluated as:

$$V_{cg} = \sum_i \tilde{\omega}(\boldsymbol{U}_g - \boldsymbol{U}_i) V_i \tag{2.8}$$

where the index i runs over the visibility values and g runs over the different grid points.

The 2d TGE is used for observations at a single frequency channel and it is an unbiased estimator of the angular power spectrum ($C(\ell)$). It can be constructed from the gridded convolved visibilities using the following expression:

$$\hat{E}_g = M_g^{-1} \left(|V_{cg}|^2 - \sum_i |\tilde{\omega}(\boldsymbol{U}_g - \boldsymbol{U}_i)|^2 |V_i|^2 \right) \tag{2.9}$$

Here the first term in the brackets is the visibility correlation while the second term is responsible for the subtraction of the noise bias. M_g is a normalization constant and is given by:

$$M_g = \left\langle \left(|V_{cg}|^2 - \sum_i |\tilde{\omega}(\boldsymbol{U}_g - \boldsymbol{U}_i)|^2 |V_i|^2 \right) \right\rangle_{UAPS} \tag{2.10}$$

where $\langle \cdots \rangle$ denotes an ensemble average over multiple realizations of the sky corresponding to a Unit Angular Power Spectrum ($C(\ell) = 1$). To calculate M_g, a sky image corresponding to a Unit Angular Power Spectrum is obtained. Then the visibilities for that sky are simulated, with the same observation parameters as the actual observation. After that, the above expression within the angular brackets is evaluated and an ensemble average is taken after repeating these steps for multiple sky realizations.

For observations with multiple frequency channels, it is necessary to consider the fact that in an actual observation, many channels will typically be flagged due to a variety of reasons. The TGE takes this into account by means of a flagging variable $F_i(\nu)$ which is 0 when the visibility is to be rejected and 1 otherwise. The gridded convolved visibilities for the 3d TGE are given by:

$$V_{cg}(\nu_a) = \sum_i \tilde{\omega}(\boldsymbol{U}_g - \boldsymbol{U}_i) V_i(\nu_a) F_i(\nu_a) \tag{2.11}$$

The expressions for the 3d TGE and the normalization grid M_g are then given as:

$$\hat{E}_g(\nu_a,\nu_b) = M_g^{-1}(\nu_a,\nu_b)\times\mathcal{R}e\left(V_{cg}(\nu_a)V_{cg}^*(\nu_b) - \delta_{a,b}\sum_i F_i(\nu_a)|\tilde{\omega}(\boldsymbol{U}_g-\boldsymbol{U}_i)|^2|V_i(\nu_a)|^2\right) \tag{2.12}$$

$$M_g(\nu_a,\nu_b) = \left\langle \mathcal{R}e\left(V_{cg}(\nu_a)V_{cg}^*(\nu_b) - \delta_{a,b}\sum_i F_i(\nu_a)|\tilde{\omega}(\boldsymbol{U}_g-\boldsymbol{U}_i)|^2|V_i(\nu_a)|^2\right)\right\rangle_{UMAPS} \tag{2.13}$$

Here M_g is evaluated in a similar manner as described for the 2d estimator, except that the sky realizations should correspond to a Unit Multifrequency Angular Power Spectrum ($C_\ell(\Delta\nu) = 1$).

2.3.3 Obtaining the Power Spectrum

The Tapered Gridded Estimator is an unbiased estimator of the MAPS, as described by equation 1.11.

$$\langle \hat{E}_g(\nu_a,\nu_b)\rangle = C_{\ell g}(\nu_a,\nu_b) \tag{2.14}$$

where $l_g = 2\pi U_g$ is the angular multipole at the g^{th} grid point. The estimator values are further binned in annular bins in the uv space in order to increase the Signal to Noise Ratio (SNR). The Binned 3d Tapered Gridded Estimator is given by:

$$\hat{E}_g[a](\nu_a,\nu_b) = \frac{\sum_g w_g E_g(\nu_a,\nu_b)}{\sum_g w_g} \tag{2.15}$$

Here w_g is the weight assigned to the g^{th} grid point. Two approaches for choosing these weights are natural weighting ($w_g = M_g$) and uniform weighting ($w_g = 1$). Natural weighting optimizes with respect to the noise while uniform weighting optimizes with respect to the cosmic variance. The binned 3d TGE is an unbiased estimator of the bin averaged MAPS:

$$C_{\ell a}(\nu_a,\nu_b) = \frac{\sum_g w_g C_{\ell g}(\nu_a,\nu_b)}{\sum_g w_g} \tag{2.16}$$

where $\ell_a = \frac{\sum_g w_g \ell_g}{\sum_g w_g}$ is the effective angular multipole in the a^{th} annulus. Under the assumption that the signal is statistically homogeneous along the frequency axis, the values corresponding to the same frequency separation can be averaged and we then

go from $C_{\ell a}(\nu_a, \nu_b)$ to $C_{\ell a}(\Delta\nu)$ where $\Delta\nu = |\nu_a - \nu_b|$. The cylindrical power spectrum can then be evaluated using the discretized version of equation 1.12:

$$\bar{P}_{k_\perp, k_{\parallel m}} = r^2 r' \Delta\nu_c \sum_{n=-N_c+2}^{N_c-1} exp(-k_{\parallel m} r' n \Delta\nu_c) C_\ell(n\Delta\nu_c) \tag{2.17}$$

where $k_{\parallel m} = \frac{m\pi}{r'_c \Delta\nu_c (N_c - 1)}$, $k_\perp = \frac{\ell}{r}$, N_c is the number of channels and $\Delta\nu_c$ is the channel width.

2.4 Foreground Mitigation

The first step in foreground mitigation pipelines is the subtraction of point sources. This should ideally be done during the calibration of the visibilities, but may also be done after obtaining an image. The MWA Real Time System [Mitchell 08] is one such pipeline which uses a method called bright source peeling during calibration. Detailed catalogues of radio sources in the field of view of the observation are often used to model and subtract the sources from the visibilities or the image. The MWA Fast Holographic Deconvolution pipeline [Sullivan 12] uses such a map to model and subtract sources. There are two common approaches used in the mitigation of the residual foregrounds: subtraction and avoidance.

Subtraction: This approach tries to model the foregrounds precisely and subtract them from the data. The early attempts at foreground subtraction used polynomial fitting to model and subtract the foregrounds. This method utilizes the fact that the foregrounds are expected to be spectrally smooth while the 21 cm signal is not. As a result, low order polynomials, fitted either to the visibilities or the image pixels, should fit only the foregrounds and leave the signal in the residuals. However, there are some serious drawbacks to this approach, the most important of them being the fact that calibration errors and polarization leakage can result in non-smooth spectra of the observed foregrounds. The methods which are used nowadays in foreground subtraction use non parametric fitting, which utilize less constrained models. The method of Gaussian Process Regression [Mertens 18] models the signal, foregrounds and noise as Gaussian processes whose covariance priors can be specified to allow some degree of control, without being too strict. Another commonly used method of non parametric foreground subtraction is Blind Source Separation. This method

models the observed signal X as X[m]=A[m,n]S[n]+N[m] where m is the number of frequency channels, S[n] are n foreground components, N is the signal with noise while the matrix A mixes the foreground components. The target is to estimate AS. Fast Independent Component Analysis (FastICA [Chapman 12]), Generalized Morphological Component Analysis (GMCA [Bobin 16]) and Correlated Component Analysis (CCA [Bonaldi 15]) are some pipelines which employ the blind source separation method for foreground subtraction. The main drawback of foreground subtraction techniques is that any error in modelling will further contaminate the data at all scales.

Foreground Avoidance: Foreground avoidance approaches attempt to avoid the region of the parameter space which have very high foregrounds. Since we expect foregrounds to be spectrally smooth, they should ideally be confined to low $k_{\parallel}$ modes. But the chromaticity of the interferometer means that a given baseline (b) probes finer spatial scales (higher $k_{\perp}$) at higher frequencies ($k_{\perp} \propto b/\lambda$). Longer baselines are more chromatic, and this effect is more pronounced at higher $k_{\perp}$. This creates a wedge like structure in the $k_{\perp}, k_{\parallel}$ space within which we would expect the foregrounds to be confined. Hence the remaining region in the k space, commonly called the EoR Window, can be used as a region relatively unaffected by foregrounds (Figure 2.1). Another approach which employs the philosophy of foreground avoidance is Delay Space Filtering [Parsons 09]. We know that the chromaticity of interferometers causes mode mixing where the spatial and spectral modes are mixed. This can be avoided if we take Fourier Transforms of the individual visibilities and work with the visibilities in the delay space. Doing this is equivalent to taking the Fourier Transform along the slanted lines instead of the vertical axis in Figure 2.1. Now, if the foregrounds are spectrally smooth, the visibilities in delay space should be close to a delta function at the position of the geometric delay between the antennas of the baseline. The geometric delay has a maximum value given by the geometric delay when the source is at the horizon and hence the foregrounds would be confined within these horizon limits. For the spectrally unsmooth 21 cm signal, however, the delta function in delay space would be convolved with a wide kernel. Hence the signal would leak out of the horizon limits and the part of the data beyond the horizon limits should be relatively less contaminated with foregrounds. Though foreground avoidance techniques do not introduce modelling errors, in avoiding the foregrounds they reject a large portion of the signal as well. This approach also prevents us from gaining access to a range of spatial frequencies which can be accessed by using foreground subtraction techniques.

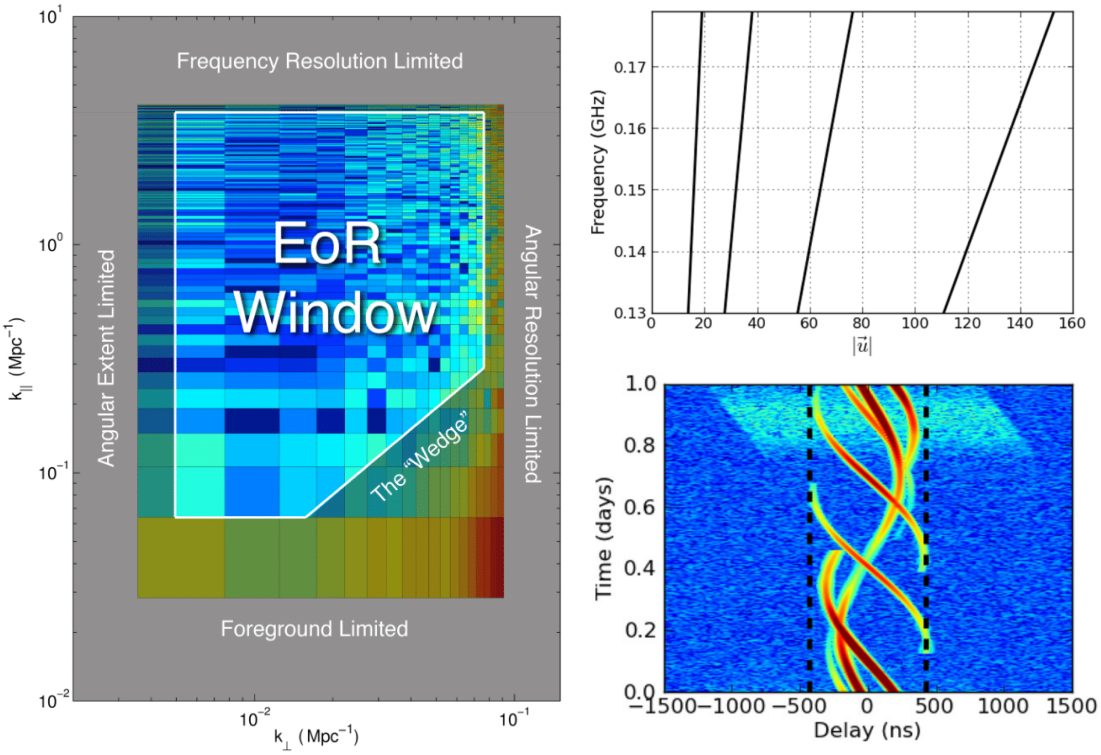

Figure 2.1: Left: The EoR window and foreground wedge in k space. (Source: Dillon et al. *Overcoming real-world obstacles in 21 cm power spectrum estimation: A method demonstration and results from early Murchison Widefield Array data*). Top Right: The variation of projected baseline vectors (and hence $k_\perp$) with frequency. Bottom Right: The foregrounds (sinusoidal curves) and the signal (diffuse emission) in the delay space. (Source: Parsons et al. *A per-baseline, delay-spectrum technique for accessing the 21 cm cosmic reionization signature*).

Chapter 3

Simulations

The aim of the first part of the project was to implement the TGE on simulated GMRT data and test its performance for different input parameters. This exercise consists of first making an image corresponding to an input power spectrum, simulating visibilities corresponding to that image for some observation parameters, followed by the implementation of the estimator and comparison of the input and recovered power spectra. This was repeated for both 2d and 3d estimators. This entire analysis was done in python 2.7 and CASA (Common Astronomy Software Applications).

3.1 Simulating Observations

The input angular power spectrum for the 2d simulations was assumed to be $C(\ell) = 513\ \mathrm{m}K^2 \times (\frac{1000}{\ell})^{2.34}$. This corresponds to the DGSE at 150 MHz measured using the GMRT [Ghosh 12]. For the 3d simulations, we assumed an input spherical power spectrum given by: $P(k) = (k/k_0)^{-2} mK^2 Mpc^3$ where $k_0 = (1.1)^{-1/2} Mpc^{-1}$ which is the same power spectrum assumed in the simulations which were used to validate the 3d TGE [Bharadwaj 19]. In order to estimate the sky image corresponding to the input power spectrum, first a grid is decided in the spatial frequency space corresponding to the desired observation parameters. The observation parameters used for the simulations are summarized in Table 3.1. The grid size was chosen to have N=65 cells along each axis. For the 2d grid in ℓ space, the maximum ℓ is given simply by $2\pi \times \mathrm{uv}_{max}$. For the 3d grid, we have $k_{\perp}^{max} = 2\pi \times \mathrm{uv}_{max}/r_{\nu_c}$ and $k_{\parallel}^{max} = N\pi/(r_{\nu_{max}} - r_{\nu_{\min}})$ where r_ν is the comoving distance at ν. Once the grid is decided, each grid cell is assigned

the value g(k).

$$g(k) = (a_k + ib_k) \times \sqrt{\frac{P(k)N^3}{2L^3}} \tag{3.1}$$

Here a_k and b_k are random numbers drawn from a Gaussian distribution with mean = 0 and standard deviation = 1. The factor of $N^3/2L^3$ (L = distance corresponding to a grid cell in image domain) is necessary to correct the normalization in the discrete Fourier Transform routine used to create the images [Bagla 97]. For the 2d grid, Equation 3.1 is replaced by:

$$g(\ell) = (a_\ell + ib_\ell) \times \sqrt{\frac{C(\ell)N^2}{2L^2}} \tag{3.2}$$

In practice, only half of the cells are filled with these values and the other half are decided by the Hermitian symmetry of the Fourier Transform of the image since the image pixel values must be real valued. Then the Inverse Fourier Transform of the grid is computed using a Fast Fourier Transform algorithm to yield the sky image. This whole procedure is repeated for the unit APS ($C(\ell) = 1$) for the 2d estimator and the unit MAPS ($C_\ell(\Delta\nu) = 1$) for the 3d estimator. $C_\ell(\Delta\nu) = 1$ implies that the $P(k) = \frac{r_\nu^2 \Delta r_\nu}{\Delta k_\parallel}\delta(k_\parallel)$ and hence the $k_\parallel = 0$ plane in the k grid is assigned this constant value for P(k) while the other cell values are 0. In this manner, the sky and normalization images corresponding to the input power spectra are obtained. Figure 3.1 shows examples of the sky and normalization images for the 2d simulations. For the 3d simulations, the sky image plane for each frequency channel is different while the normalization image plane for each channel has the same noise distribution. These images, along with the observation parameters and the GMRT antenna distribution stored in a configuration file are then given as input to the CASA simulator tool which returns the simulated visibilities in the form of a Measurement Set (MS). The UV coverage of the 2d simulations is shown in Figure 3.1.

Parameter	Value
RA	10h46m00s
Dec	59d00m59s
ν_c	150 MHz
Bandwidth	16 MHz
UV range	10 to 1000
Observation Period	-4 hr to +4 hr
Integration Time	10 min

Table 3.1: Observation Parameters used for the simulations.

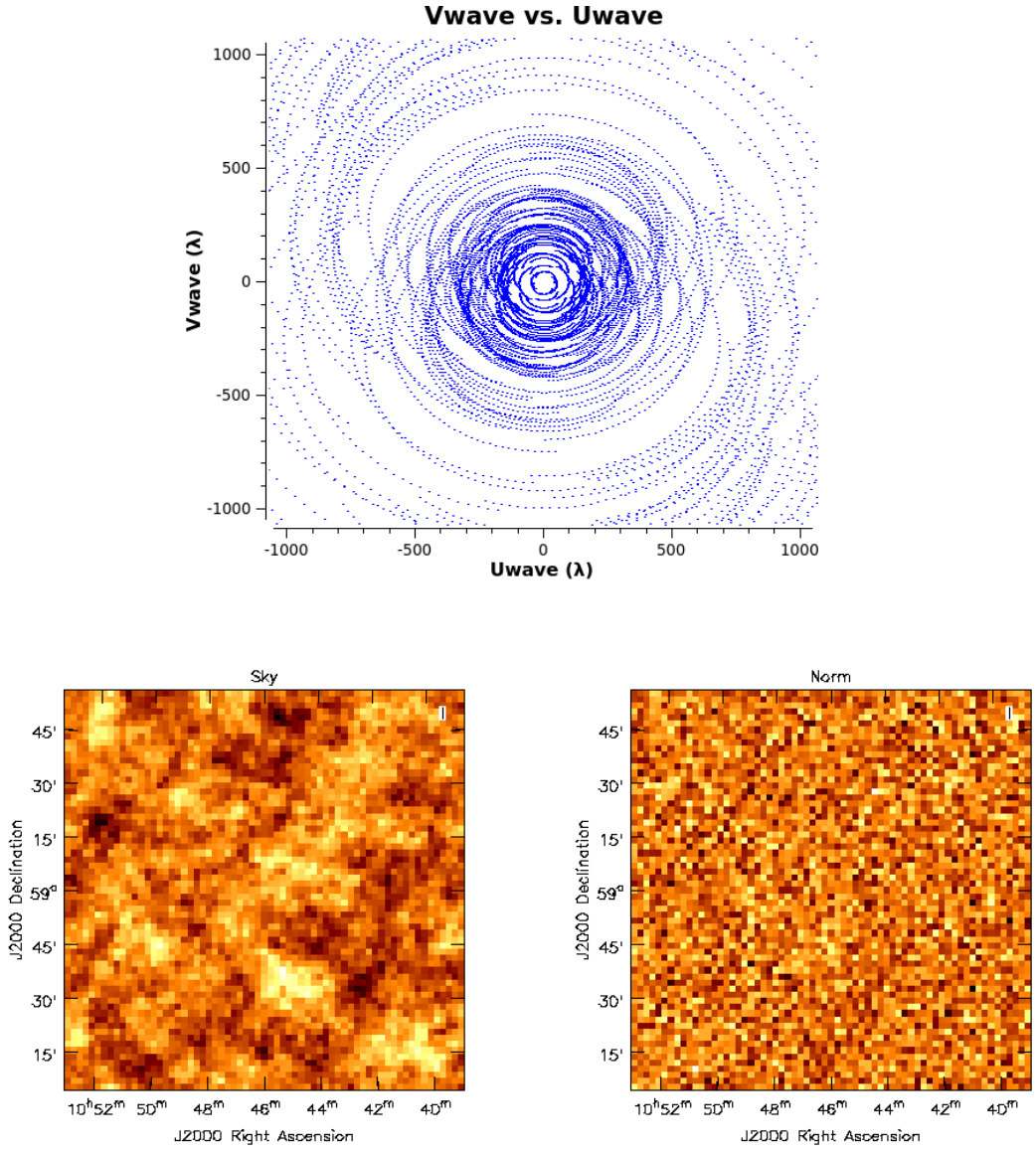

Figure 3.1: UV coverage and example images for the 2d simulations. Top: UV coverage. Bottom Left: Sky image. Bottom Right: Normalization Image.

3.2 Applying the Estimator

As discussed in 2.3.2, the first step is to choose a window function which will be used to taper the sky response. For this analysis, a Gaussian window function was chosen, with a Full Width at Half Maximum (FWHM) of 57 arcmin which is about one third of the GMRT primary beam FWHM at 150 MHz (FWHM $\approx \frac{1.03\lambda}{D} \approx 157$ arcmin). This is Fourier Transformed analytically to get the tapering window in uv space. Then a uniform grid in the uv space is chosen between uv_{min} and uv_{max}. The gridded convolved visibilities are then calculated using Equation 2.8 (for 2d) and Equation 2.11 (for 3d).

The above steps are repeated for the visibilities simulated using the normalization image and the simulations are themselves repeated for multiple normalization images. Then the normalization matrix is constructed using Equation 2.10 (for 2d) and Equation 2.13 (for 3d), by taking an ensemble average of the grid values across 10 different realizations of the normalization image. This part of the code, where multiple normalization images are used to simulate and construct multiple normalization grids, is parallelized to reduce the computation time.

These gridded convolved visibilities and the M_g are then used to construct the $\hat{E}_g$ matrix using Equation 2.9 (for 2d) and Equation 2.12 (for 3d). In this way, the normalized estimator grid is constructed. Figures 3.2 and 3.3 illustrate the grids for the 2d simulations.

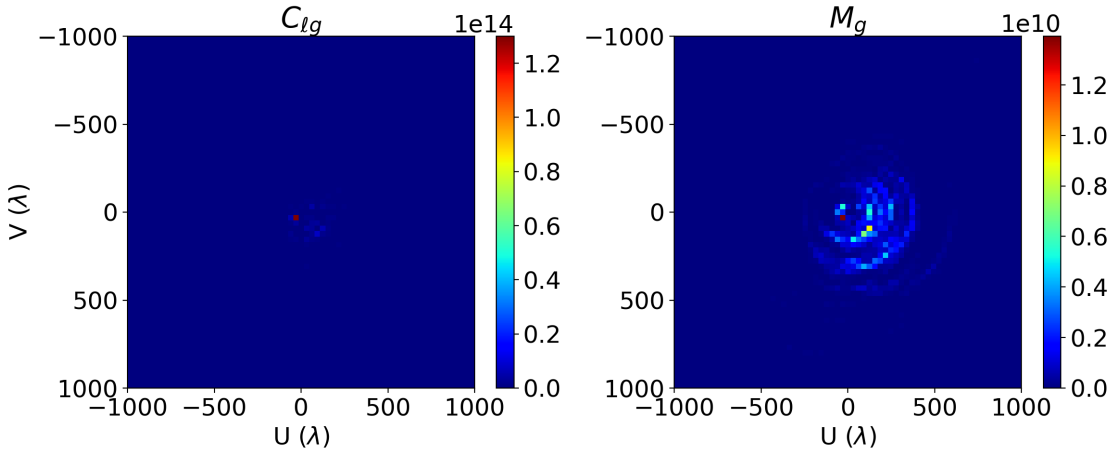

Figure 3.2: Grids for 2d simulations. Left: $\hat{E}_g \times M_g$, Right: M_g.

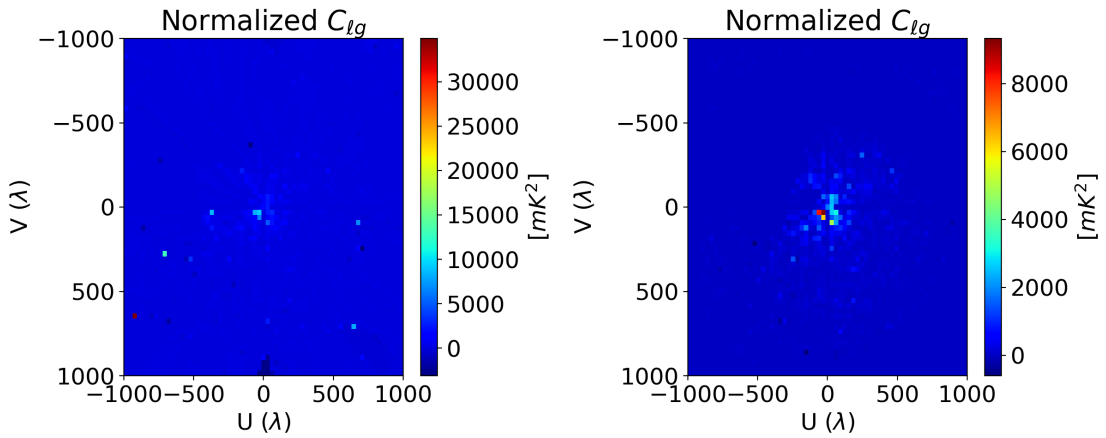

Figure 3.3: Normalized estimator grids for 2d simulations. Left: $\hat{E}_g$ for natural weighting. Right: $\hat{E}_g$ for uniform weighting.

The next step involves specifying annuli within which we want to average the estimator values (Equation 2.15). For this analysis, 9 equally spaced annuli were used, between uv=100 and uv=1000. Since some grid points will not be sampled by the GMRT baseline distribution, while uniformly weighting the estimator values, only those grids which have a value of $M_g > 10^5$ were used. For natural weighting, the grid cells which are not sampled are automatically given small weights and this step is not necessary.

The averaged estimator values directly yield the $C(\ell)$ (for 2d) and $C_\ell(\nu_a, \nu_b)$ (for 3d). For the 3d estimator, the different estimator planes with the same $\Delta\nu$ are averaged to give $C_\ell(\Delta\nu)$. Figures 3.4 and 3.5 show the obtained APS and MAPS respectively. The input $C_\ell(\Delta\nu)$ for the 3d simulations has been calculated by taking an inverse Fourier Transform of the input P(k). We see that there seems to be an underestimation of the recovered APS at low ℓ values. The plots for the MAPS also show underestimation and dips in the residuals for the lower ℓ values as seen in Figure 3.5. This can be expected since these lower ℓ values will be affected more by sample variance. All the plots that will be shown from this point onwards are for natural weighting. Uniform weighting gives very similar plots.

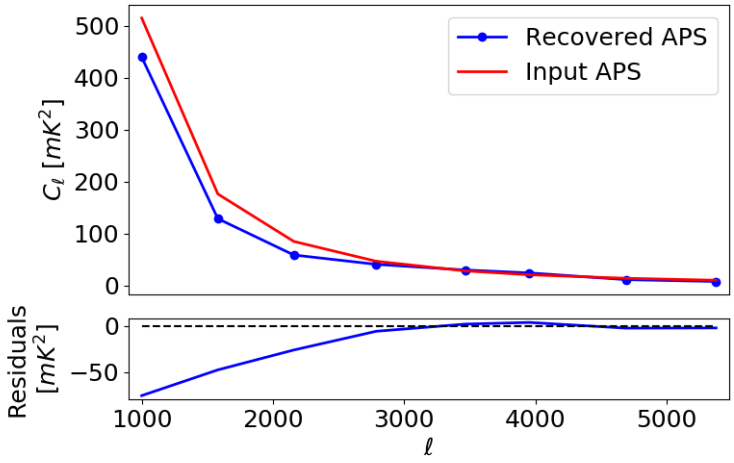

Figure 3.4: The recovered and input APS.

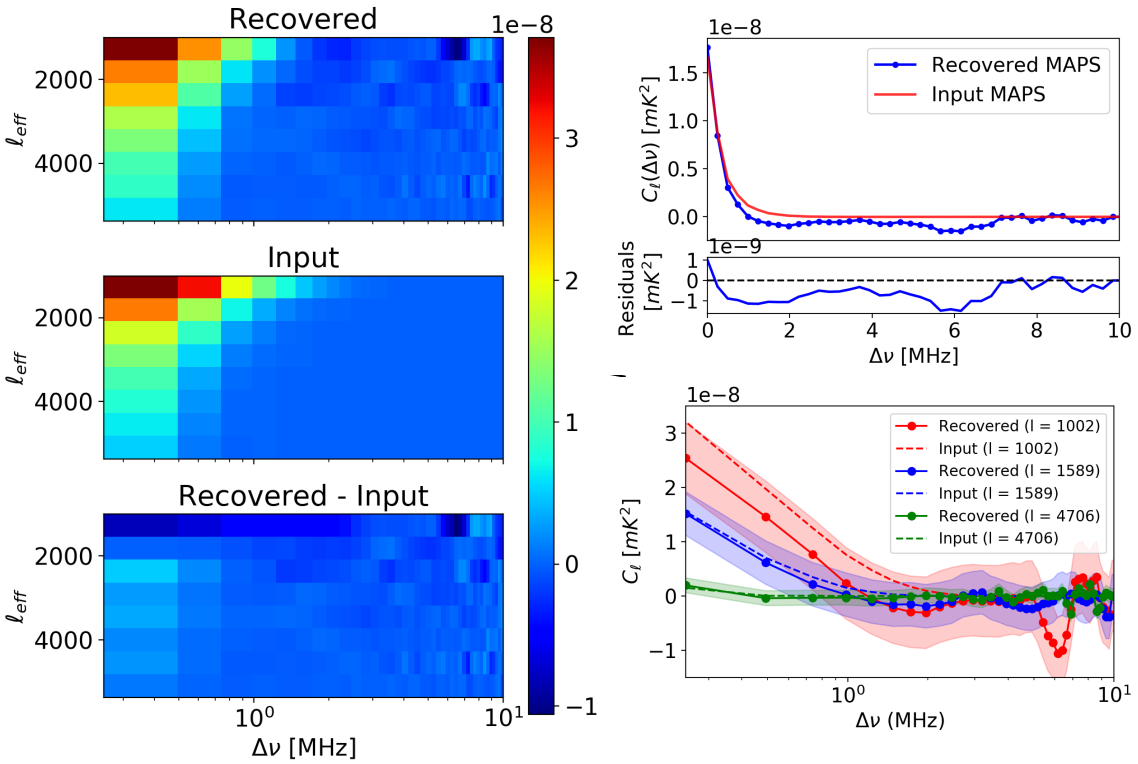

Figure 3.5: Left: The MAPS as a function of both ℓ_{eff} and $\Delta\nu$. Top right: MAPS averaged across ℓ values plotted against $\Delta\nu$. Bottom right: The MAPS for a few specific ℓ values plotted against $\Delta\nu$. The shaded regions indicate the 1σ deviations.

For the 3d simulations, there is one more step of obtaining the cylindrical and spherical power spectra. The cylindrical power spectrum is obtained using Equation 2.17 on the

estimated MAPS. The corresponding plots are shown in Figure 3.6. The cylindrical power spectra are further averaged in spherical shells in k space of constant width, to obtain the spherical power spectrum. We see that at low k values there is a significant underestimation of the power spectrum, while for the majority of the k range, the power spectrum is overestimated.

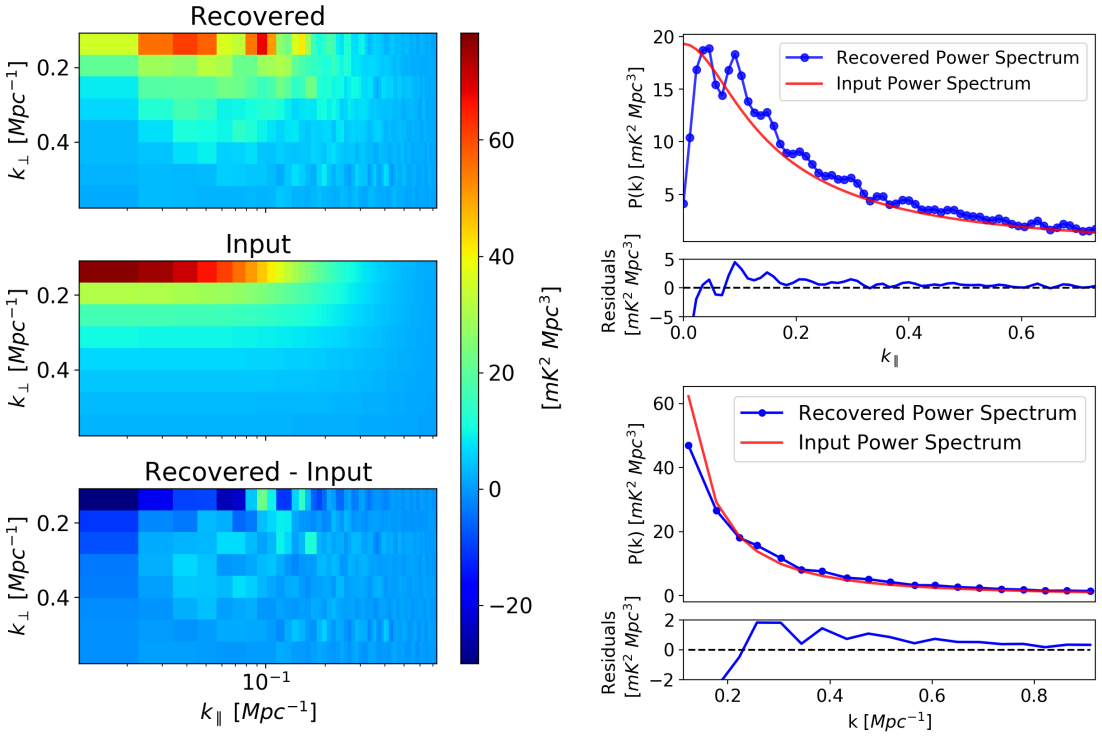

Figure 3.6: Left: The cylindrical power spectra as a function of both $k_\perp$ and $k_\parallel$. Top right: The 1d profile with the power for $k_\perp$ values averaged. Bottom right: The input and recovered spherical Power Spectra.

3.3 Testing the Estimator's Performance

The results described in 3.2 correspond to a single realization of the sky and we do not have error bars on the measurements which tell us how the power spectrum estimation might change for a different sky realization corresponding to the same input power spectrum. In order to test the performance of the estimator for different situations, these error bars are necessary. To get an estimate of the error bars, the entire analysis in 3.2 was repeated for an ensemble of sky realizations. This part of the code, where the estimators for different sky realizations are computed, was again parallelized to reduce the computation time. The results for the 2d and 3d estimators are presented

in Figure 3.7. In these plots $\langle \cdots \rangle$ denotes an ensemble average and the error bars correspond to the maximum and minimum values obtained across the different sky realizations.

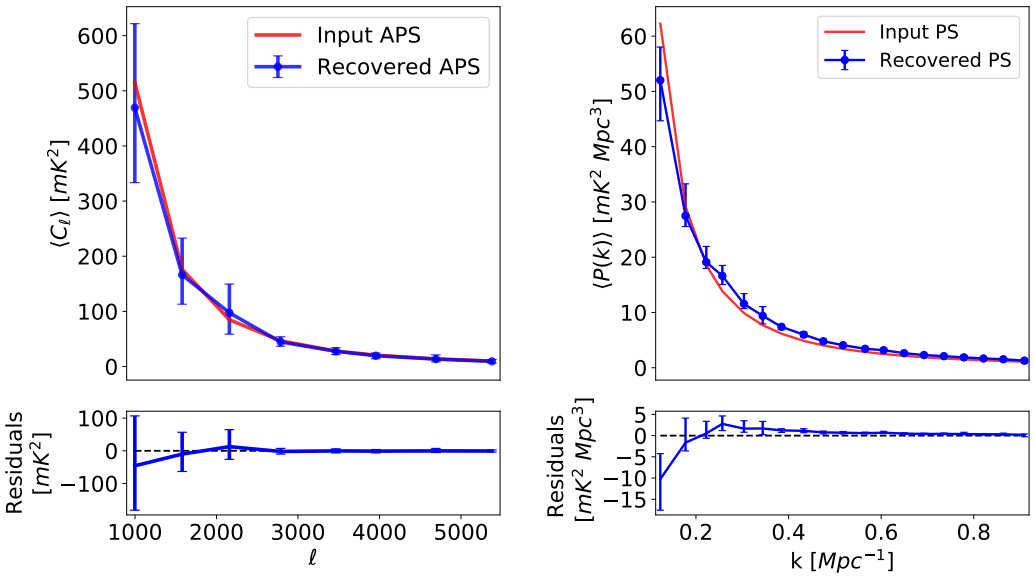

Figure 3.7: Left: The mean APS. Right: The mean spherical PS.

To test the effect of noise on the performance of the estimator, after constructing the sky image, Gaussian noise was added to the visibilities. Then the above analysis was repeated for multiple sky realizations and the plots with error bars were obtained. This was then repeated for different input values of noise. Now the mean of the deviations of $\langle C(\ell) \rangle$, $\langle C_\ell(\Delta\nu) \rangle$ and $\langle P(k) \rangle$ from their input values gives us an estimate of the accuracy of the estimator. The mean value of the error bar lengths gives us an estimate of the effect of sample variance on the performance of the estimator. So these two quantities are plotted against the input noise in Figure 3.8. From the plots, it seems that uniform weighting results in more overestimation than natural weighting, for both 2d and 3d simulations. The cause for this overestimation for uniform weighting could be the fact that we need to select a threshold M_g value while binning the estimator values in annuli. Also, the effect of sample variance becomes more severe as the input noise is increased. Figure 3.9 shows an example of how adding noise affects the $C_\ell(\Delta\nu)$ and $P(k_\perp, k_\parallel)$.

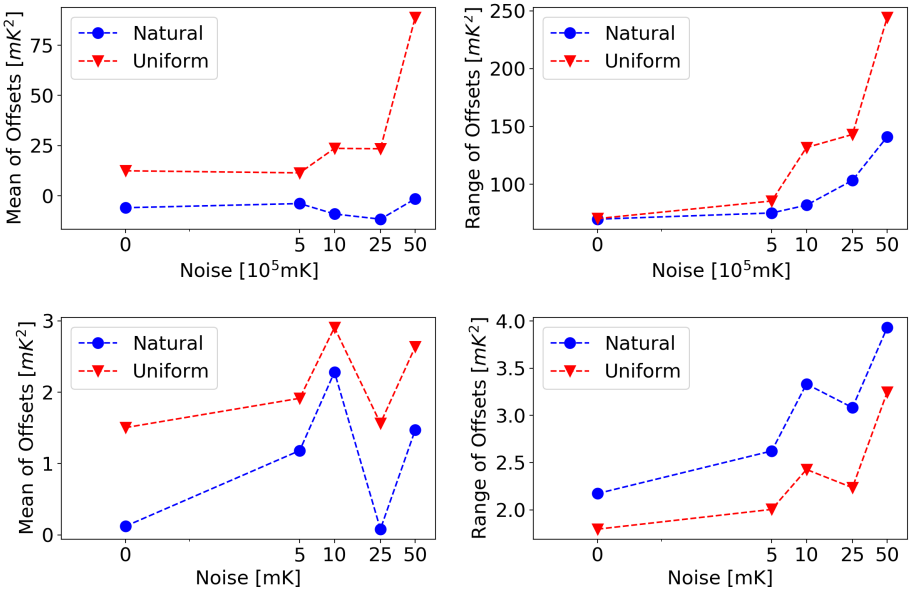

Figure 3.8: Plots showing accuracy of the estimator (left) and effect of sample variance on the estimator (right) as a function of input noise. The top row is for the 2d estimator and the bottom row for the 3d estimator.

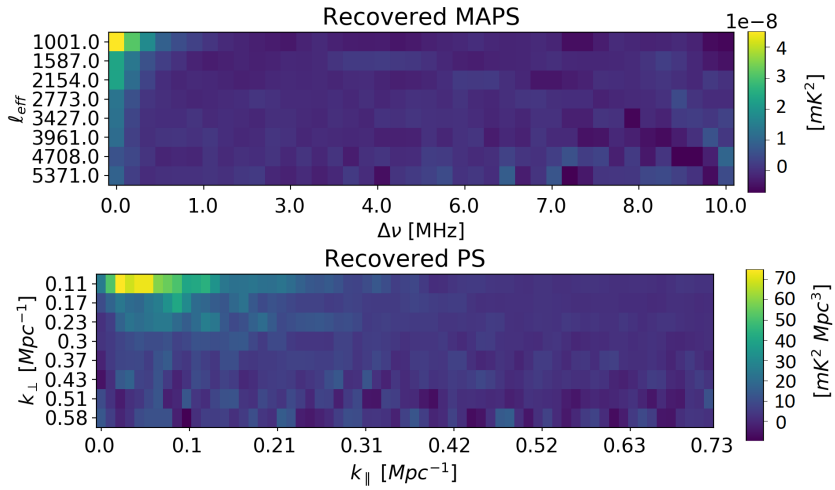

Figure 3.9: Top: The recovered MAPS when noise is added to visibilities. Bottom: The corresponding cylindrical PS.

To test the effect of sparsity of the antenna distribution on the performance of the estimator, a similar analysis was done. The simulations for multiple sky realizations were repeated for different number of antennas used and the set of antennas to be used in each case was chosen at random. Finally, plots similar to Figure 3.8 for accuracy and effect of sample variance were obtained, but as a function of number of antennas. These plots are shown in Figure 3.10. For the 2d estimator, the deviation becomes

more positive as the antenna distribution becomes sparse. For 3d estimator, we see a trend of increased effect of sample variance for more sparse configurations. The other two plots, range of offsets for 2d estimator and mean of offsets for 3d estimator, do not show any specific trend and have not been shown here.

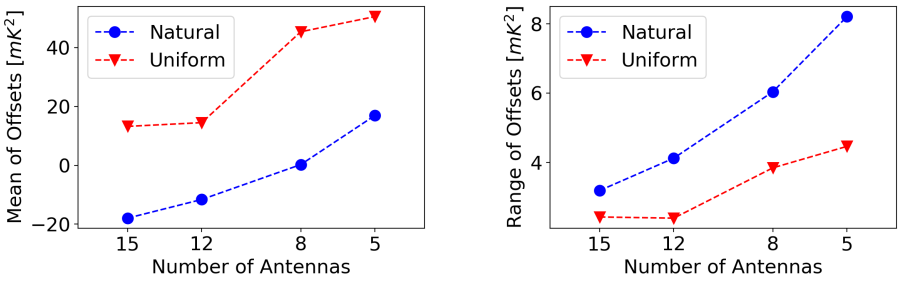

Figure 3.10: Plots showing accuracy of the 2d estimator (left) and effect of sample variance on the 3d estimator (right) against the number of antennas.

3.4 Summary

Following is a brief summary of the analysis described in this chapter:

- The 2d and 3d TGE are applied to simulated GMRT observations and they recover the input power spectra reasonably well. Both the 2d and 3d estimator show an underestimation of the recovered power spectra at low ℓ and k. This is possibly due to the absence of very small baselines in the GMRT antenna distribution. At high k, for the 3d estimator, there is an overestimation and this decreases as k increases.
- Uniform weighting results in higher values of the estimated power spectra than natural weighting. Adding noise to the visibilities increases the effect of sample variance on the performance of the estimator.

Chapter 4

GMRT Observations

The Giant Metrewave Radio Telescope (GMRT) is a radio interferometric array located near Pune, India [Swarup 91]. It is one of the largest radio arrays in the world and consists of 30 dish antennas, each having a diameter of 45m. The array of antennas is in a "Y" configuration, consisting of a central compact square and three extended arms. The compact square contains 14 antennas distributed randomly, while the remaining antennas form the arms of the Y shape. The antennas in the central square are the ones most important for intensity mapping, since the smaller baselines of upto 1 Km will be particularly sensitive to extended structures in the sky. The GMRT can observe in a frequency range from 50 MHz to 1500 MHz with a maximum instantaneous bandwidth of 400 MHz.

4.1 EGS Data

The Extended Groth Strip (EGS) is a small patch of the sky between the constellations of Ursa Major and Boötes and is one of the darkest and most dust free regions of the sky. The central region of the field was observed using the GMRT and reduced with both the GMRT Software Backend (GSB) and the GMRT Wideband Backend (GWB). For the GSB data, phase, flux and bandpass calibration and flagging of Radio Frequency Interference (RFI) affected data was done by Pranav Kukreti for his Master's thesis where he used radio stacking analysis to study the star formation rate (SFR) of typical star forming galaxies at z=0.028. The GWB data was reduced by Apurba Bera [Bera 19] to study SFR at intermediate redshifts ($0.2 < z < 0.4$). In

this analysis, we have used these calibrated visibilities for HI intensity mapping.

Since the python codes used for the simulations in the previous chapter are computationally slow, the codes developed by the IIT Kharagpur team were used for obtaining the MAPS and Power Spectra of the large volume of EGS data. These codes have a few changes to what was described in section 2.3. The first of these changes is that in Equation 2.12, the Kronecker delta is no longer present. This is equivalent to lifting the assumption that the noise in different frequency channels will not be correlated. It is seen that this becomes necessary in actual data, in the presence of foregrounds since this assumption results in a dip in the recovered MAPS at $\Delta\nu = 0$ [Pal 21]. Another change is introduced in the step where the estimated $C_\ell(\Delta\nu)$ is Fourier Transformed to obtain the cylindrical power spectrum. Instead of an FFT algorithm to compute the Fourier Transform, a Maximum Likelihood Estimator has been used for the purpose [Pal 21]. This is useful since the $C_\ell(\Delta\nu)$ values are better estimated for lower values of $\Delta\nu$. The inverse of Equation 2.17 is written in matrix notation as:

$$C_\ell(n\Delta\nu_c) = \sum_m A_{nm}\bar{P}(k_\perp, k_{\parallel m}) + [Noise]_n \tag{4.1}$$

where A is the Hermitian matrix containing the Fourier Transform coefficients and n,m go from 0 to $N_c - 1$. The maximum likelihood estimate of the power spectrum is:

$$\bar{P}(k_\perp, k_{\parallel m}) = \sum_n [(A^\dagger N^{-1} A)^{-1} A^\dagger N^{-1}]_{mn} C_\ell(n\Delta\nu_c) \tag{4.2}$$

where N is the noise covariance matrix. This approach gives the necessary weight to $\Delta\nu$ values which have lower associated noise and hence is a better alternative to the standard FFT method.

4.2 Analysis - GSB Data

The GSB dataset has observations of the EGS on 12 nights, totalling 57 on-source hours. The observations are centred at an observation frequency of 1381.2 MHz and the visibilities have 510 frequency channels, with a bandwidth of 33.33 MHz.

4.2.1 Results - Individual Nights

The initial analysis consisted of applying the TGE to individual nights separately and obtaining the MAPS and Power Spectra for the same. This was done with the objective of testing the quality of the data on each night and checking the consistency and errors of the obtained power spectra across nights. The analysis was repeated for two tapering windows, with f=0.8 and f=3 to study the effect of tapering. Here f is the fraction by which the tapering window FWHM is smaller than the FWHM of the GMRT primary beam. Figure 4.2 shows the plots of $C_\ell(\Delta\nu)$ against $\Delta\nu$ for the individual observation nights. We see oscillations whose frequency increases as we increase the ℓ value. For large ℓ values, slower oscillations also begin to be seen. These are expected to come from point sources near the first null of the primary beam. The sharp dips at large $\Delta\nu$ are effects of systematics at the edge channels. Figure 4.3 shows the spherical power spectra for the different nights. While making this plot, the values of the power spectrum in the range $k_\perp > 15$ have been averaged in spherical k shells with logarithmic binning. The limit in $k_\perp$ is chosen since the convolution is expected to dominate at large angular scales. This results in a minimum value of ℓ given by $\ell_{min} = 1823.72 \times \frac{\sqrt{1+f^{2.5}}}{f^{1.25}}$ [Choudhuri 14] which equals $\ell = 3022$ for f=0.8 and $\ell = 1881$ for f=3. This corresponds to roughly the six smallest ℓ and hence $k_\perp$ bins. The results seem to be fairly consistent and all the nights have been used for the subsequent analysis. The 4 shorter observations have not been plotted because they deviate substantially from the mean. This is likely since the uv coverage for these 4 observations is very patchy. The comparison between the uv coverage for the longest observation night and that for the entire observation has been shown in Figure 4.1. This reveals that using the full observation will give us access to more k modes.

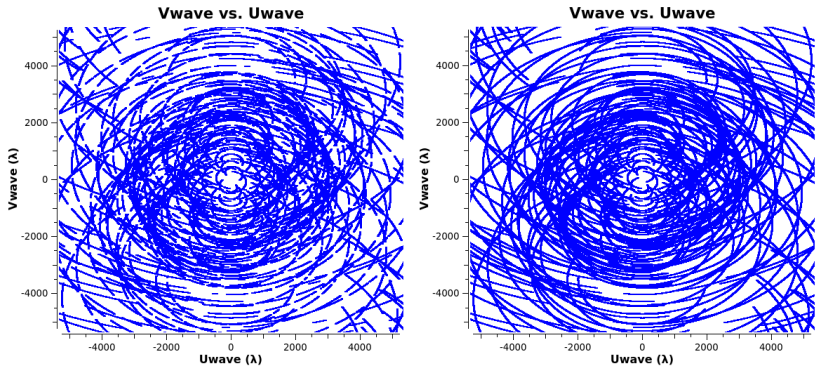

Figure 4.1: UV Coverage (single channel) for the longest individual observation night (left) and that for the full observation (right). Only values less than 5000 have been shown in both plots.

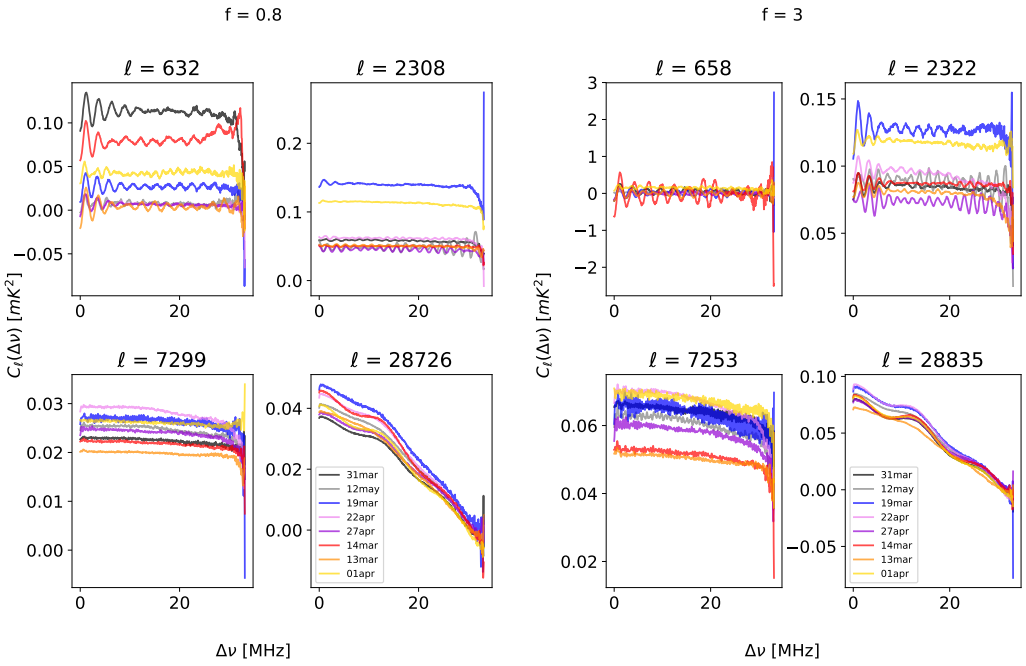

Figure 4.2: $C_\ell(\Delta\nu)$ against $\Delta\nu$ for 4 different ℓ values, for the 8 longest observation nights for f=0.8 (left) and f=3 (right). The dates in the legend go from the longest to shortest observation as we go from top to bottom.

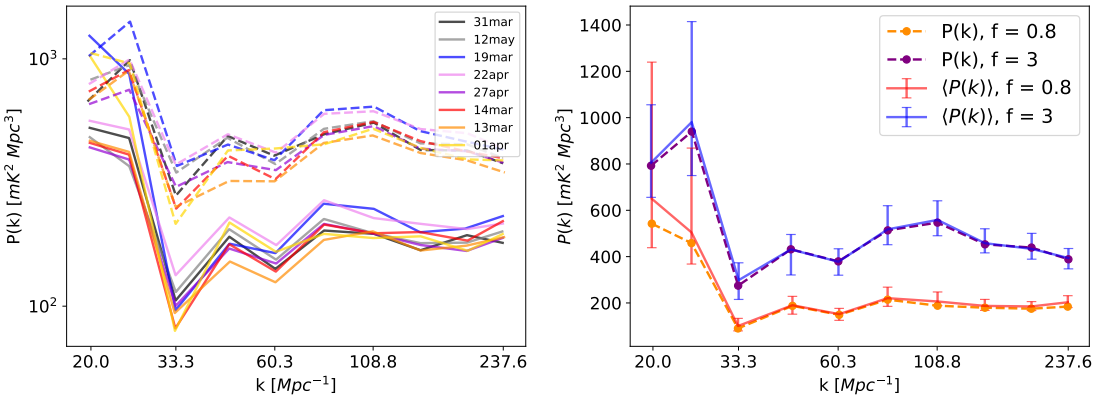

Figure 4.3: Left: Spherical power spectra for the 8 longest observation nights. The dashed lines are for f=3 and the solid lines are for f=0.8. Right: Spherical power spectra for the entire observation (dashed lines) over-plotted with the ensemble average of power spectra over the 8 individual nights. The error bars correspond to the maximum and minimum power values across the 8 nights.

4.2.2 Results - Full Observation

The visibilities for the 12 nights of observation were concatenated and the edge channels were removed from the data to avoid systematics. The final visibility dataset contains 461 channels and the percentage of flagged data is about 9%. The MAPS and Power spectra for this entire observation was obtained for f=0.8 and f=3. A visual inspection of the dirty image for the observation reveals the field to be dominated by 7 bright point sources. The positions of these sources match with those of the 7 brightest sources in the AEGIS20 catalogue that fall in this field. Table 4.1 lists the position and integrated flux values for these sources in the AEGIS20 catalog and for this observation. To model the point sources, the tclean task in CASA was used. A deep continuum image was made using Briggs weighting and robust=-0.5. The point source model produced after cleaning was Fourier Transformed into the visibility plane and subtracted from the calibrated visibilities. The subtracted visibilities were checked for artefacts due to cleaning and the clean parameters were modified with the aim of minimizing the cleaning artefacts near the brightest source, where they are expected to be the most prominent. In total, 39 sources were subtracted so that there are no sources in the residual data with a peak flux density of above 120 μJy. The noise in the image is $\sigma = 17$ μJy and hence all sources above 7σ have been modelled and subtracted. Each source was cleaned to a depth of 1.5σ while making the model. Figure 4.4 shows the cleaned image with point sources and the dirty image after point source subtraction.

Observation			Catalogue		
RA	Dec	Flux	RA	Dec	Flux
14:20:33.8	53:00:04	53.31	14:20:33.3	53:00:04	58.55
14:19:46.0	52:46:47	8.53	14:19:45.5	52:46:48	10.59
14:21:04.0	52:56:51	5.06	14:21:03.6	52:56:51	7.98
14:19:11.0	52:48:30	4.19	14:19:10.4	52:48:31	6.07
14:19:46.6	52:56:48	2.12	14:19:46.1	52:56:47	3.12
14:21:01.2	52:54:25	1.79	14:21:00.8	52:54:25	2.22
14:18:44.6	52:57:37	0.69	14:18:44.2	52:57:36	1.73

Table 4.1: RA, Dec and Integrated flux values (in mJy) for the seven brightest sources in the image and the sources in the AEGIS20 catalogue that fall in this field.

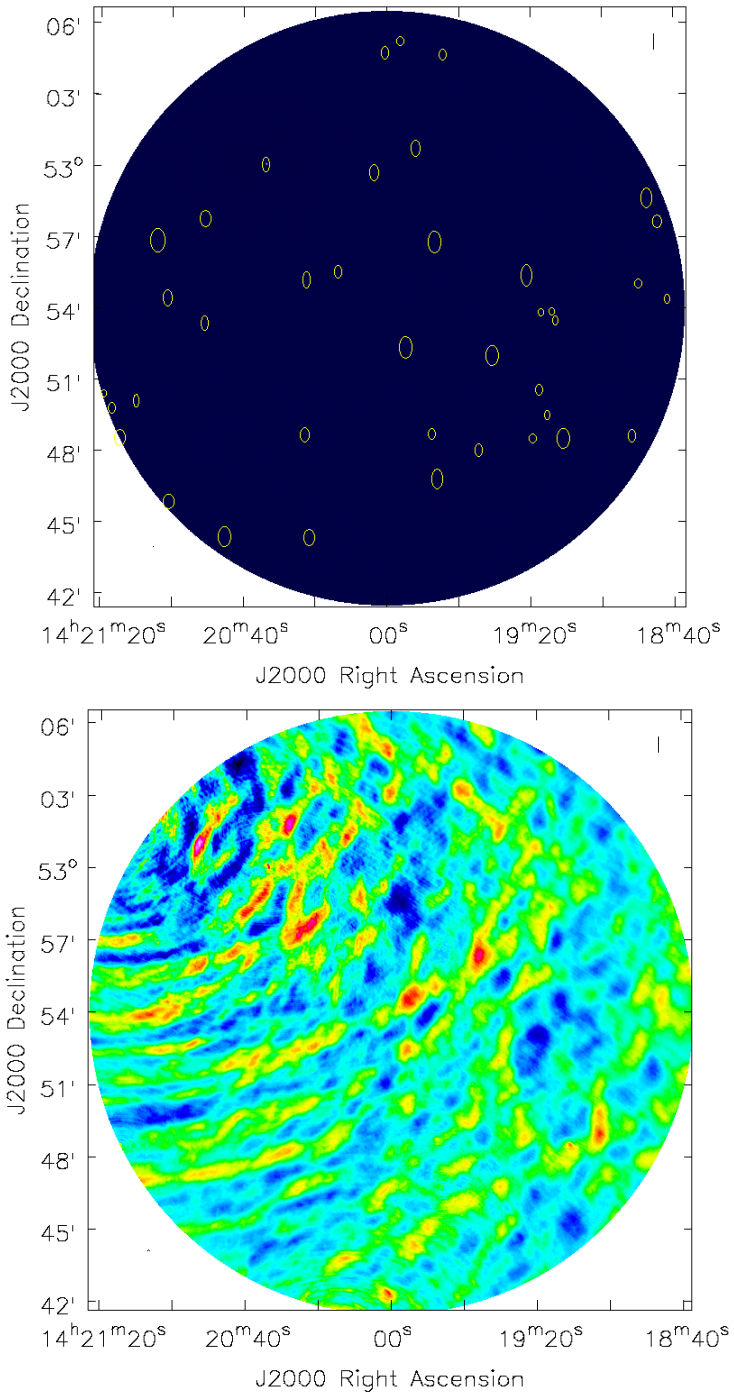

Figure 4.4: Top: Cleaned image (high resolution) for full observation. The 39 sources that were subtracted are marked in circles. Bottom: Dirty image (low resolution) after point source subtraction.

In order to understand the effect of point source subtraction on the resulting power spectra, the TGE was applied to the visibilities both before and after point source subtraction with two different tapering fractions of f=0.8 and f=3. The 2d TGE was

applied to the dataset averaged across the frequency channels to estimate the angular power spectrum. For this purpose, a uv range of 400 to 50,000 was chosen with 50 logarithmic bins. The results are shown in 4.5. The effect of point source subtraction is evident, and it results in decrease in power. The DGSE, which is expected to dominate the foreground contribution after point source subtraction, has a $T \propto \nu^{-2.8}$ dependence on frequency [Platania 03]. In previous studies, the $C(\ell)$ has been found to have values $\approx 10^4 mK^2$ at $\ell \approx 10^4$ and at 150 MHz[Ghosh 12]. This would imply a value of $\approx 10^{-2} mK^2$ at our observation frequency and hence, the magnitude of the APS seems to be roughly consistent with these predictions.

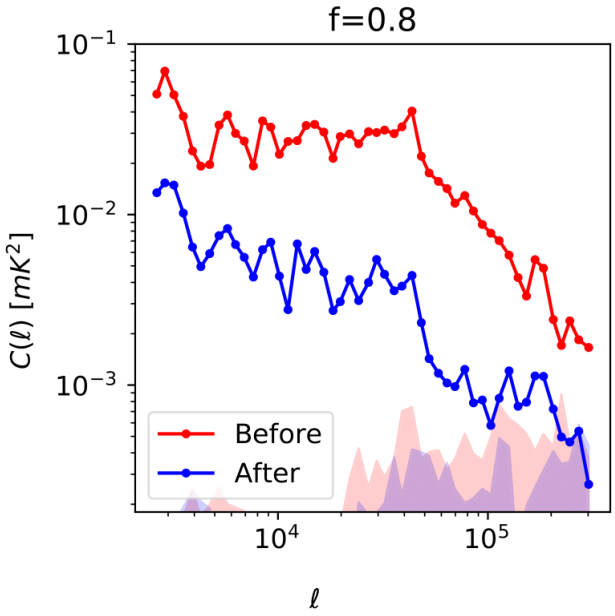

Figure 4.5: The Angular Power Spectra before and after point source subtraction, with f=0.8. The shaded regions correspond to 100σ errors due to system noise.

For the 3d TGE, the baselines in the range $100 \leq$ uv ≤ 5000 were used, which corresponds to maximum baseline length of $\approx$ 1.1 Km. This would include only the central square of antennas of the GMRT in the analysis and these set of short baselines would sample the shortest $k_\perp$ modes, and hence are most sensitive to large scale structures. 16 realizations of $M_g(\nu_a, \nu_b)$ were used to compute the ensemble averaged normalization matrix. While obtaining the binned $C_\ell(\Delta\nu)$, $P(k_\perp, k_\parallel)$ and P(k), logarithmic binning has been used in the uv and k space. To get an estimate of the error bars on the measurements due to the system noise, the following approach was used. The standard deviation of the visibilities (σ_N) is calculated. The values obtained for σ_N are 399.2 mJy and 397.9 mJy before and after source subtraction respectively.

Then visibilities are simulated corresponding to the observation parameters, but with mean=0 and standard deviation=σ_N. This is repeated 16 times to get 16 such simulated noise datasets. The simulated datasets are used to obtain the MAPS and PS in the same manner as the original observation and the standard deviation across the 16 realizations is used as an estimate of the error in the measured values arising due to system noise.

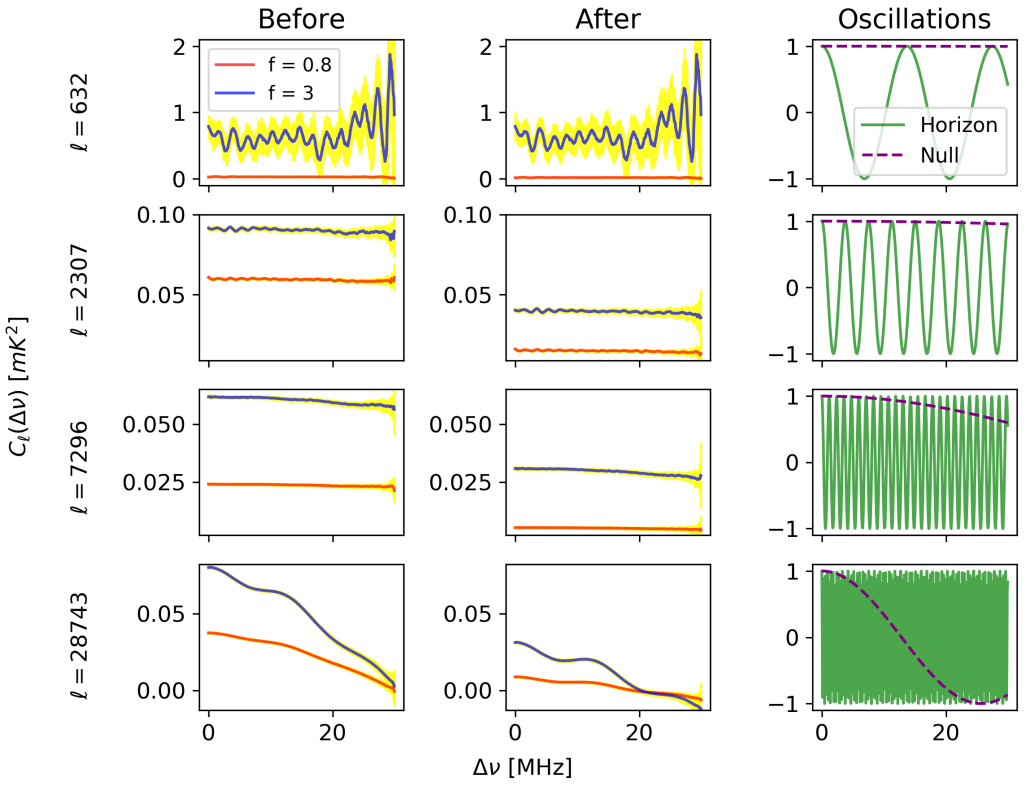

Figure 4.6: MAPS for 4 different ℓ values before and after source subtraction, for f=3 and f=0.8. The right panel illustrates the frequency oscillations expected due to point sources located at the null and the horizon. The shaded regions in yellow indicate the 50σ errors due to noise.

Figure 4.6 illustrates the effect of point source subtraction and tapering on $C_\ell(\Delta\nu)$. In the lowest ℓ plot, strong oscillations are seen and the frequency of these oscillations increase with ℓ. The dips in $C_\ell(\Delta\nu)$ at large $\Delta\nu$ are no longer present and they must have been an effect of systematics in the edge channels. At higher ℓ values, a slower oscillation sets in which could be the effect of sources near the null. Point source subtraction has negligible effect on the lower ℓ values, but significantly decreases the amplitude of $C_\ell(\Delta\nu)$ at higher ℓ.

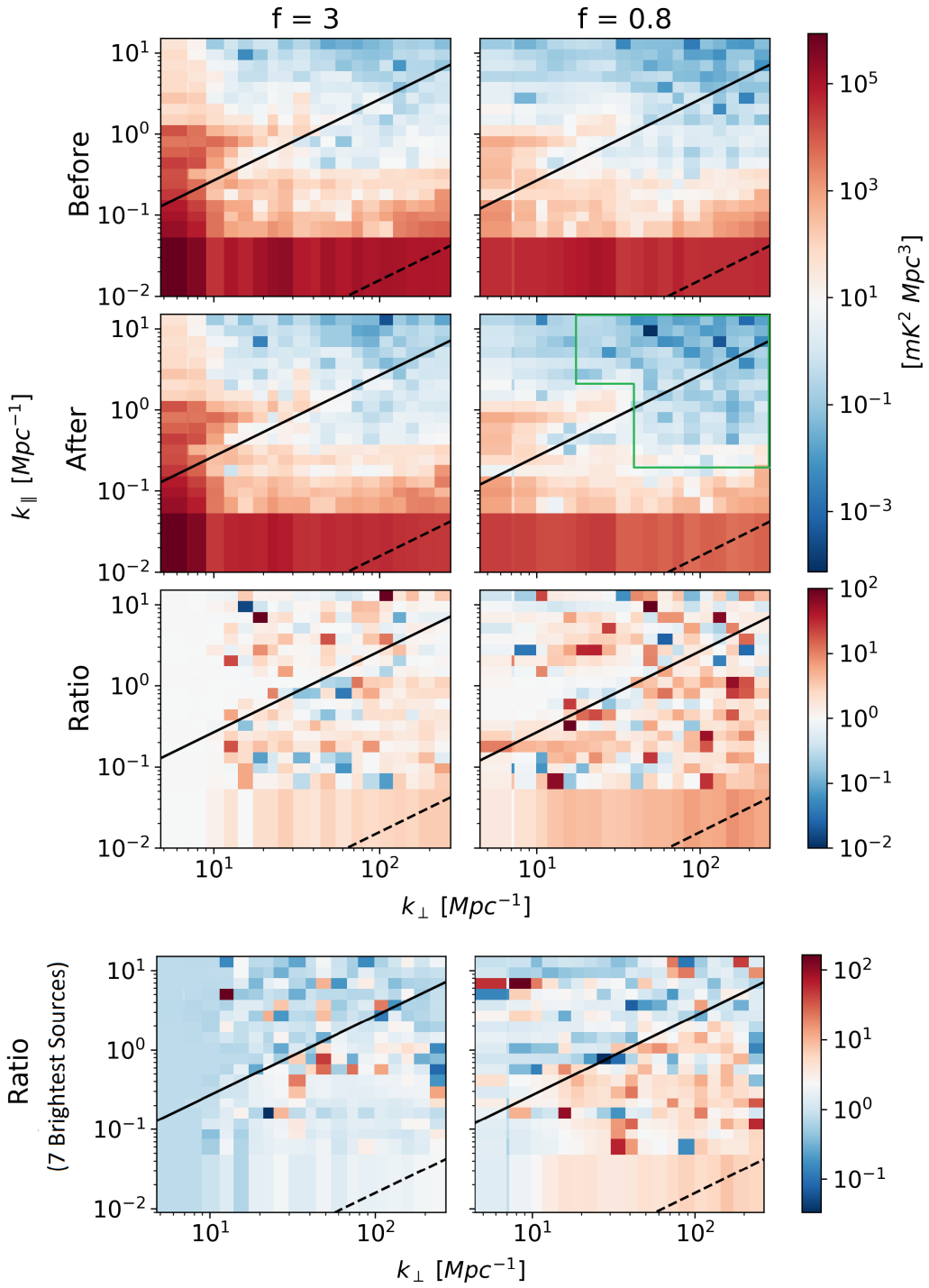

Figure 4.7: The absolute value of the cylindrical PS before and after source subtraction, for f=3 and f=0.8. The 3rd panel from top is the plot of the ratio of the PS before and after point source subtraction. The bottom panel shows the "Ratio" plot when only 7 brightest sources were subtracted. The solid line and dashed black lines are the horizon and first null limits respectively.

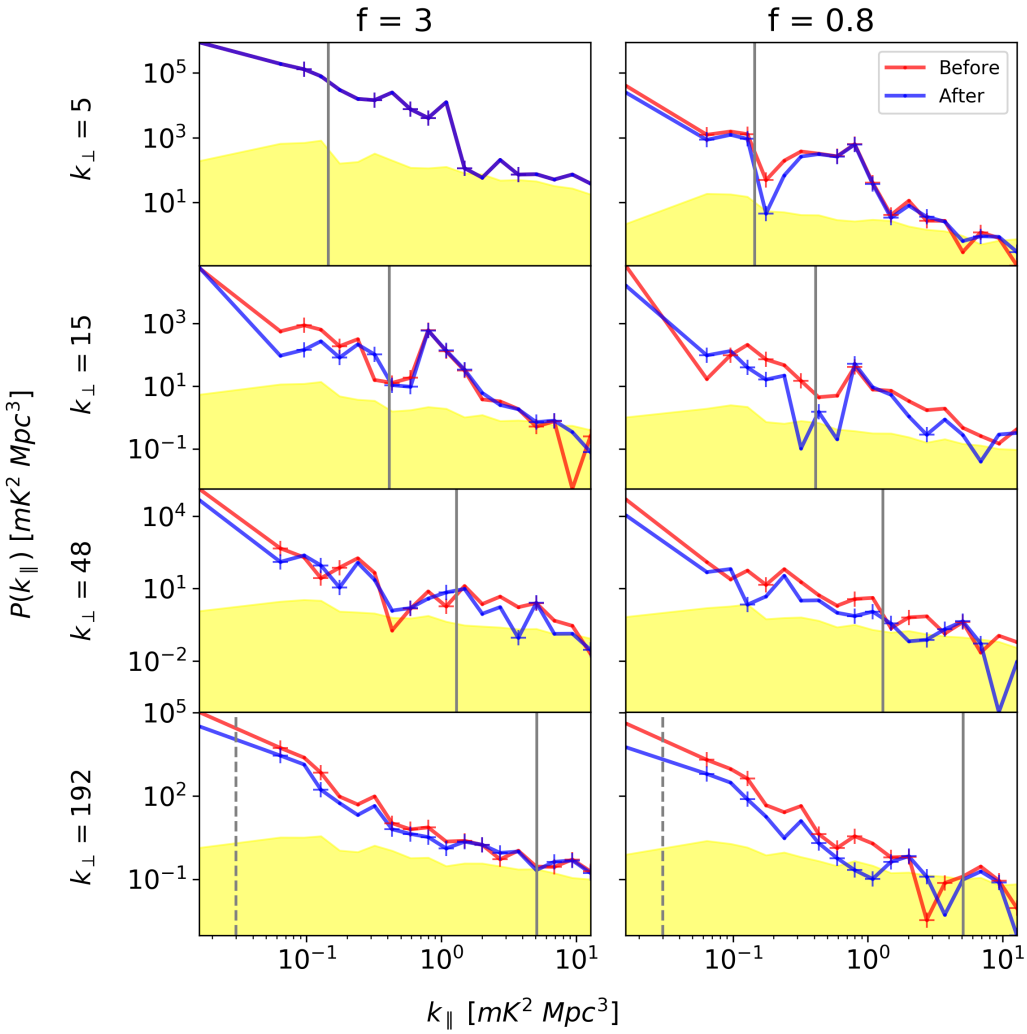

Figure 4.8: The absolute value of $P(k_\perp, k_\parallel)$, plotted against $k_\parallel$ at 4 different $k_\perp$ values. The negative values are indicated with "+" symbols. The grey dashed and solid lines are the first null and horizon limits respectively. The yellow shaded regions are the 1σ errors due to noise, after point source subtraction.

Figure 4.7 is a plot of the absolute value of the cylindrical power spectrum. We see that for $k_\perp < 10$, tapering is effective in suppressing the foregrounds, while point source subtraction does not have too much of an effect. The large $k_\perp$ and $k_\parallel$ modes are the ones less affected by foregrounds and these regions have been used for obtaining the spherical power spectra. The large number of values > 1 in the "Ratio" plot indicates that point source subtraction removes power on an average, and seems to have a stronger effect on the lowest $k_\parallel$ modes. If instead of 39 sources, only the 7 brightest sources are subtracted, we see an effective subtraction only within the horizon limits. This could be because the stronger sources have a smoother spectrum and hence do

not leak beyond the wedge. The region enclosed by the green lines in the 2nd row right column in Figure 4.7 is now used as a region relatively clean of foregrounds.

To observe how the power varies with source subtraction and tapering as we increase $k_\parallel$, $P(k_\perp, k_\parallel)$ is plotted against $k_\parallel$ for a few $k_\perp$ values in Figure 4.8. We see that the power drops off by several orders of magnitude as we go from the smallest to the largest $k_\parallel$ bin. But we do not see any such trend along $k_\perp$. Point source subtraction decreases the power and the effect is more pronounced at small $k_\parallel$. At the smallest few $k_\perp$ values, the effect of point source subtraction is very less. Tapering the sky response reduces the powers in most of the $k_\perp$ values, but the effect does not seem to be very pronounced.

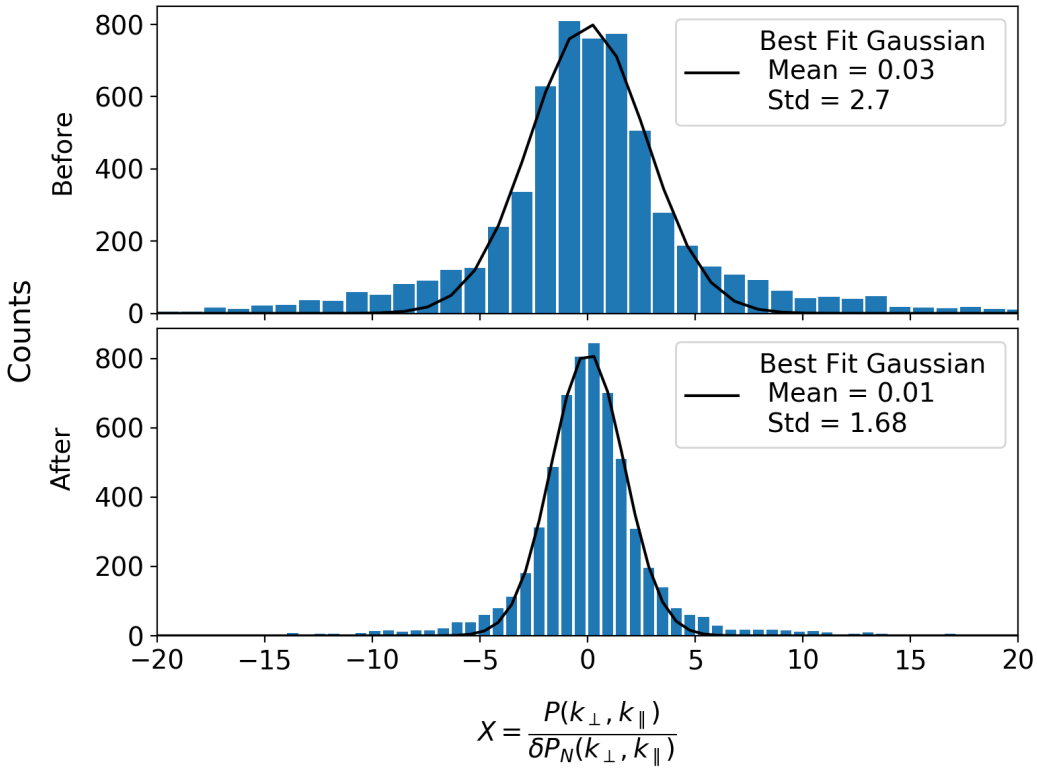

Figure 4.9: The histogram of the function $X = \frac{P(k_\perp,k_\parallel)}{\delta P_N(k_\perp,k_\parallel)}$ for f=0.8 in the window indicated in the 2nd row right column in Figure 4.7.

Next, the quantity $X = \frac{P(k_\perp,k_\parallel)}{\delta P_N(k_\perp,k_\parallel)}$ is computed in the selected region. In the absence of foregrounds or the signal, X should follow a Gaussian distribution with mean $(\mu(X))$ = 0 and standard deviation $(\sigma(X))$ = 1. A deviation of $\mu(X)$ from 0 indicates the presence of residual foregrounds while a deviation of $\sigma(X)$ from 1 indicates that the distribution of the errors in measured power values differs from that expected due

to the system noise alone. The values of $\mu(X)$ and $\sigma(X)$ are estimated by fitting a Gaussian to a histogram of X values. Before point source subtraction, we get $\mu(X) = 0.03$, $\sigma(X) = 2.7$ and after point source subtraction we get $\mu(X) = 0.01$, $\sigma(X) = 1.68$. $\mu(X) > 0$ indicates that residual foregrounds are present in the region, but they are reduced after point source subtraction. $\sigma(X) > 1$ indicates that the $\delta P_N(k_\perp, k_\parallel)$ underestimate the actual statistical fluctuations in $P(k_\perp, k_\parallel)$ by a factor of $\sigma(X)$. Figure 4.9 shows the histograms of X before and after point source subtraction for f=0.8.

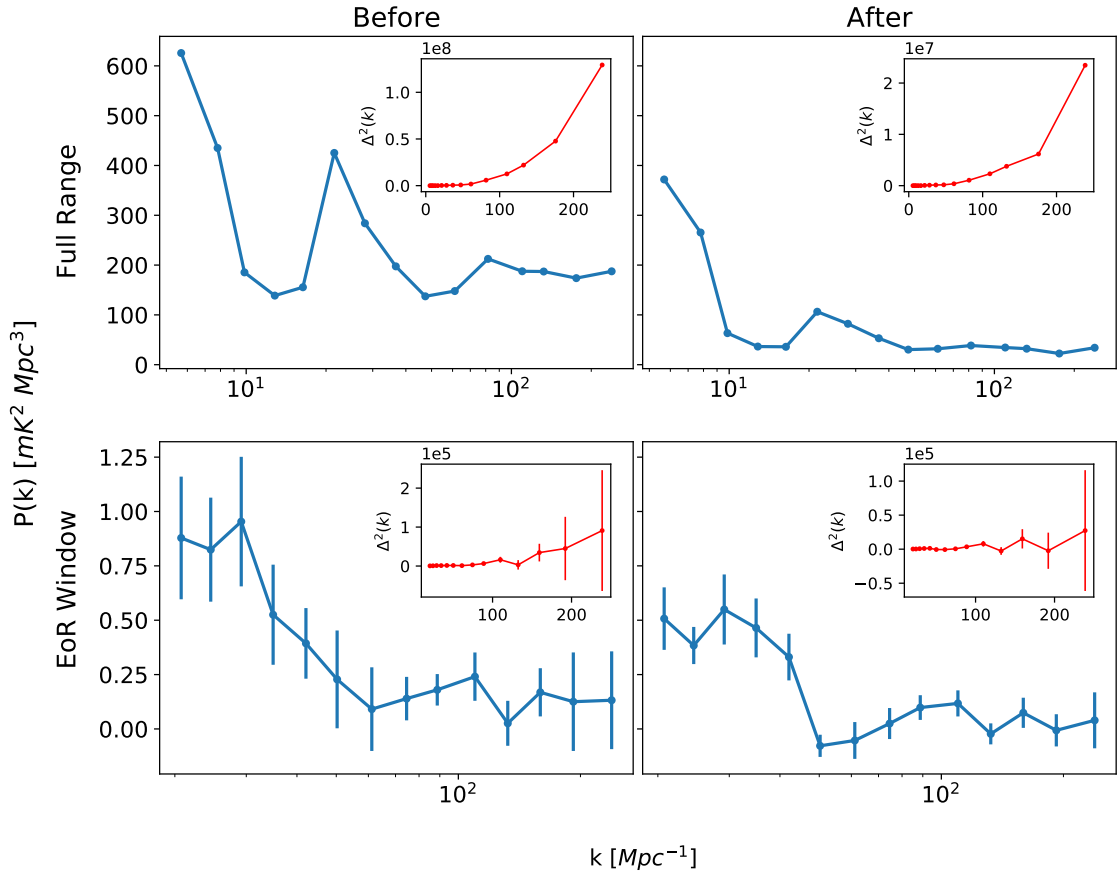

Figure 4.10: Spherical PS before and after point source subtraction, for f=0.8. The top panel is when the values in the entire k range are used to compute the spherical PS. The bottom panel shows the results when only a region in the EoR window as indicated in the 2nd row right column in Figure 4.7. Plots of $\Delta^2(k)$ against k are shown as insets in the corresponding panels.

The region indicated in Figure 4.7 was used to bin the power values in spherical shells in k space with logarithmic binning. The results for f=0.8 are shown in Figure 4.10. The error bars correspond to $2 \times \sigma(X) \times \delta P_N$ where δP_N is the error expected

due to system noise and $\sigma(X)$ is the factor by which this estimate underestimates the standard deviation of the actual distribution of errors. We see that the power decreases when we subtract point sources and this decrease in more pronounced when the binning is done in the full k range relative to when it is done in the window. After point source subtraction, at high k, the values fluctuate around zero and in this region, the noise seems to dominate the foregrounds. The dimensionless power spectrum is defined as $\Delta^2(k) = k^3P(k)/2\pi^2$ and the plots of $\Delta^2(k)$ against k are also shown in Figure 4.10.

4.2.3 Contraints on $\Delta^2(k)$ and $\Omega_{HI}b_{HI}$

The values obtained for $\Delta^2(k)$ for f=0.8, after point source subtraction and in the region in k space relatively free of foregrounds can now be used to set upper limits on the magnitude of the dimensionless power spectrum at these scales and at a redshift of 0.028. Defining the 2σ upper limit for the dimensionless power spectrum as $\Delta^2_U(k) = \Delta^2(k) + 2\sigma$ [Mertens 20], these limits are computed and the results are summarized in 4.2. In the table, only the k values below $50Mpc^{-1}$ have been listed since we appear to reach the noise limit after that and get both positive and negative values of $\Delta^2(k)$.

The 21 cm power spectrum is linked to the dark matter power spectrum through Equation 1.8. Converting the power spectra to dimensionless power spectra, we rewrite Equation 1.8 as:

$$\Delta^2_{HI}(k,z) = \bar{T}(z)^2 \times b^2_{HI} \times \Delta^2_{DM}(k,z) \tag{4.3}$$

where $\Delta^2_{DM}(k,z) = \frac{k^3 P_{DM}(k,z)}{2\pi^2}$ and $\bar{T}(z)$ is given by [Anderson 18]:

$$\bar{T}(z) = 0.39\frac{\Omega_{HI}}{10^{-3}}\left[\frac{\Omega_m + \Omega_\Lambda(1+z)^{-3}}{0.29}\right]^{-1/2}\left[\frac{1+z}{2.5}\right]^{1/2} mK \tag{4.4}$$

k $[Mpc^{-1}]$	$\Delta^2(k)$ $[mK^2]$	σ $[mK^2]$	$\Delta^2_U(k)$ $[mK^2]$
20.73	$(15.13)^2$	$(5.69)^2$	$(17.14)^2$
24.52	$(16.93)^2$	$(5.65)^2$	$(18.71)^2$
29.16	$(26.26)^2$	$(10.06)^2$	$(29.87)^2$
34.94	$(31.68)^2$	$(12.09)^2$	$(36.01)^2$
42.09	$(35.34)^2$	$(14.24)^2$	$(40.67)^2$

Table 4.2: Upper limits on the dimensionless power spectrum at z = 0.028.

The python Large Scale Structure toolkit (nbodykit [Hand 18]) was used to simulate

the linear dark matter power spectrum in the observed redshift and k bins using a linear model. Equation 4.3 is then used to obtain upper limits to the quantity $\Omega_{HI} \times b_{HI}$. Table 4.3 lists the calculated limits on $\Omega_{HI} b_{HI}$.

k $[Mpc^{-1}]$	20.73	24.52	29.16	34.94	42.09
$\Omega_{HI} \times b_{HI}$ $[10^{-2}]$	1.79	1.90	2.96	3.47	3.81

Table 4.3: Upper limits on the the quantity $\Omega_{HI} \times b_{HI}$ at z = 0.028.

Previous measurements suggest that $\Omega_{HI} \approx 3.9 \times 10^{-4} h_{70}^{-1}$ [Jones 18]. The value of the linear bias b_{HI} is taken to be 1. Using these values and Equations 4.3 and 4.4, we can construct the predicted HI dimensionless power spectrum. The plots of $\Delta^2_U(k)$ and $\Delta^2_{HI}(k)$ are shown in Figure 4.11. The estimated upper limits are seen to be at least 3 orders of magnitude more than the predicted power spectrum.

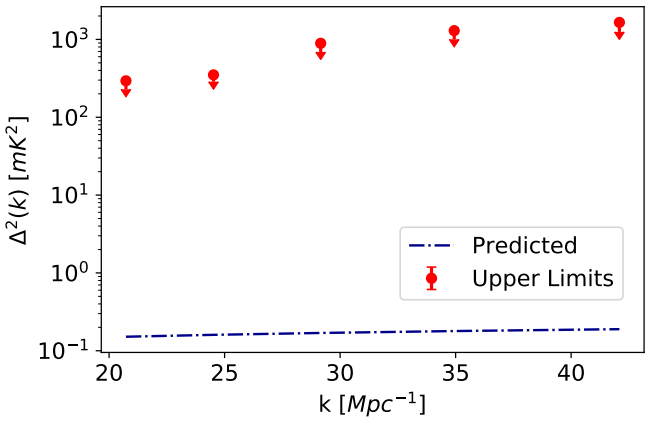

Figure 4.11: The estimated $\Delta^2_U(k)$ and predicted $\Delta^2_{HI}(k)$.

4.3 Analysis - GWB Data

We have used a small section of the GWB data for the analysis. This dataset was recorded during March-April 2017 in the uGMRT observation cycle 31 and covers a frequency range of 1001 to 1084 MHz. The data is divided into two subsets: 1001-1048 MHz and 1036-1084 MHz with a frequency resolution of 97.6 kHZ. The two datasets were calibrated together and the central square baselines were not used during the calibration. The UV data is continuum subtracted, down to $\approx 30\mu$Jy. The data reduction was done by Apurba Bera for his work on start formation rate at intermediate redshifts [Bera 19]. In our analysis, we apply the TGE separately to the two sets of calibrated visibilities, after rejecting the edge channels.

4.3.1 Results

Since tapering the sky response was seen to be effective in suppressing foregrounds in case of the GSB data, a tapering parameter of f=0.8 is used in this analysis. For the z=0.34 data (corresponding to a central frequency of 1060 MHz), a uv range of 100 to 18000 has been used while for the z=0.38 data (corresponding to a central frequency of 1025 MHz), the uv range has been chosen to be 100 to 17000. These ranges correspond roughly to a maximum baseline length of 5 Km. The MAPS, Cylindrical PS and the Spherical PS are evaluated and noise simulations are used to get error bars on the measurements, in the same manner as described in the previous section for the GSB data analysis.

Figure 4.12 is a plot showing the uv coverage in the uv range used for the analysis of the z=0.34 and z=0.38 datasets. The dense uv coverage due to the central square antennas can be identified in the plots.

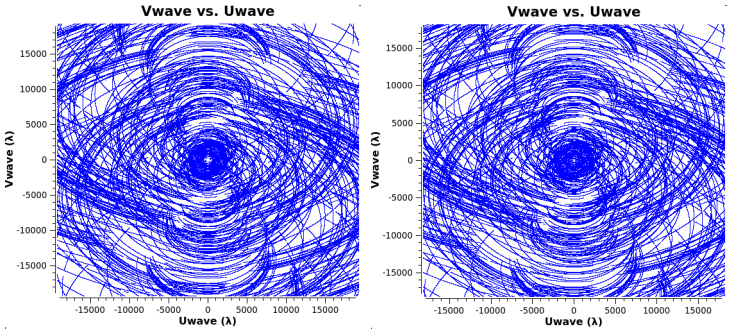

Figure 4.12: UV Coverage (single channel) for the z=0.34 and z=0.38 datasets.

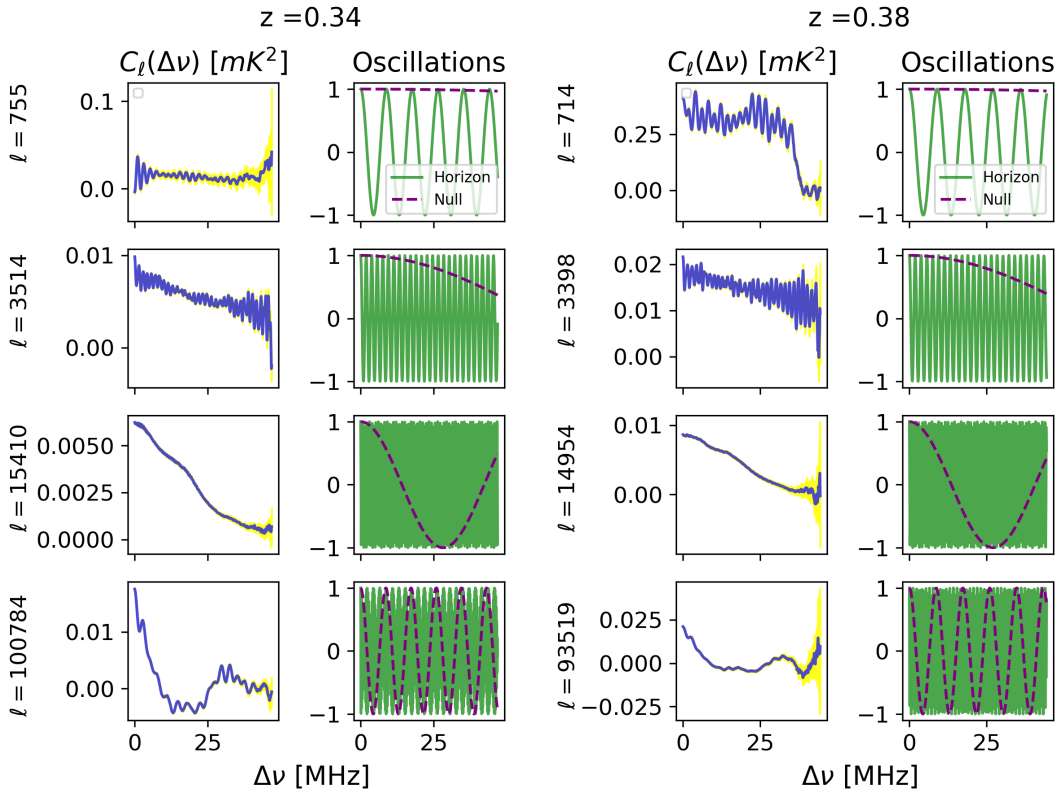

Figure 4.13: $C_\ell(\Delta\nu)$ for z=0.34 and z=0.38 plotted against $\Delta\nu$ at 4 different ℓ values. The yellow shaded regions correspond to the 50σ errors due to system noise.

Figure 4.13 is a plot of the MAPS at 4 different ℓ values. The oscillations in the MAPS increase in frequency with increasing ℓ and at large ℓ, a slower oscillation from sources near the null sets in. These observed features seem to be fairly consistent with the frequency of oscillations expected from sources near the first null and horizon.

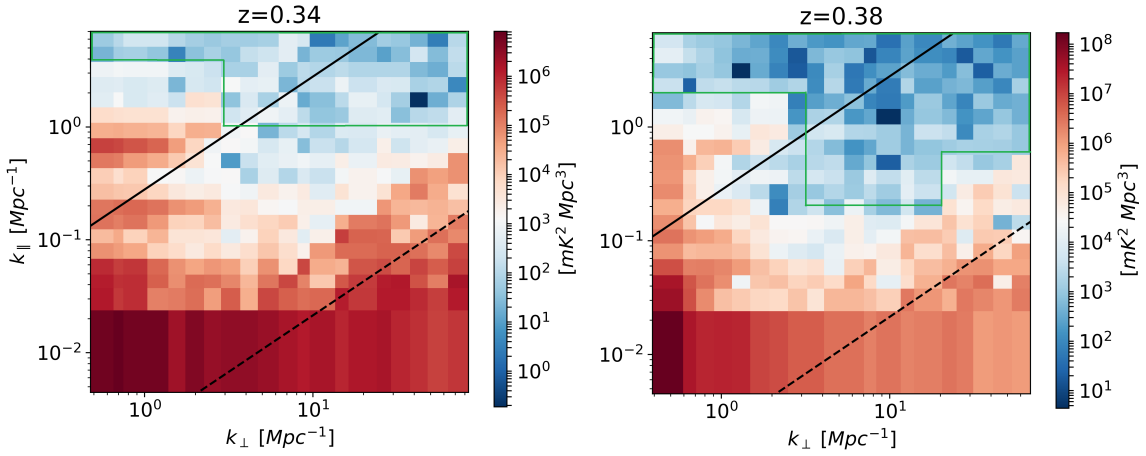

Figure 4.14: Absolute value of the cylindrical PS at z=0.34 and z=0.38.

Figure 4.14 shows the cylindrical power spectra and for both z=0.34 and z=0.38, we see a clear foreground wedge. The region marked within green lines are considered as regions relatively less contaminated by foregrounds. The power values in these regions are used to construct the spherical power spectrum and histogram of X.

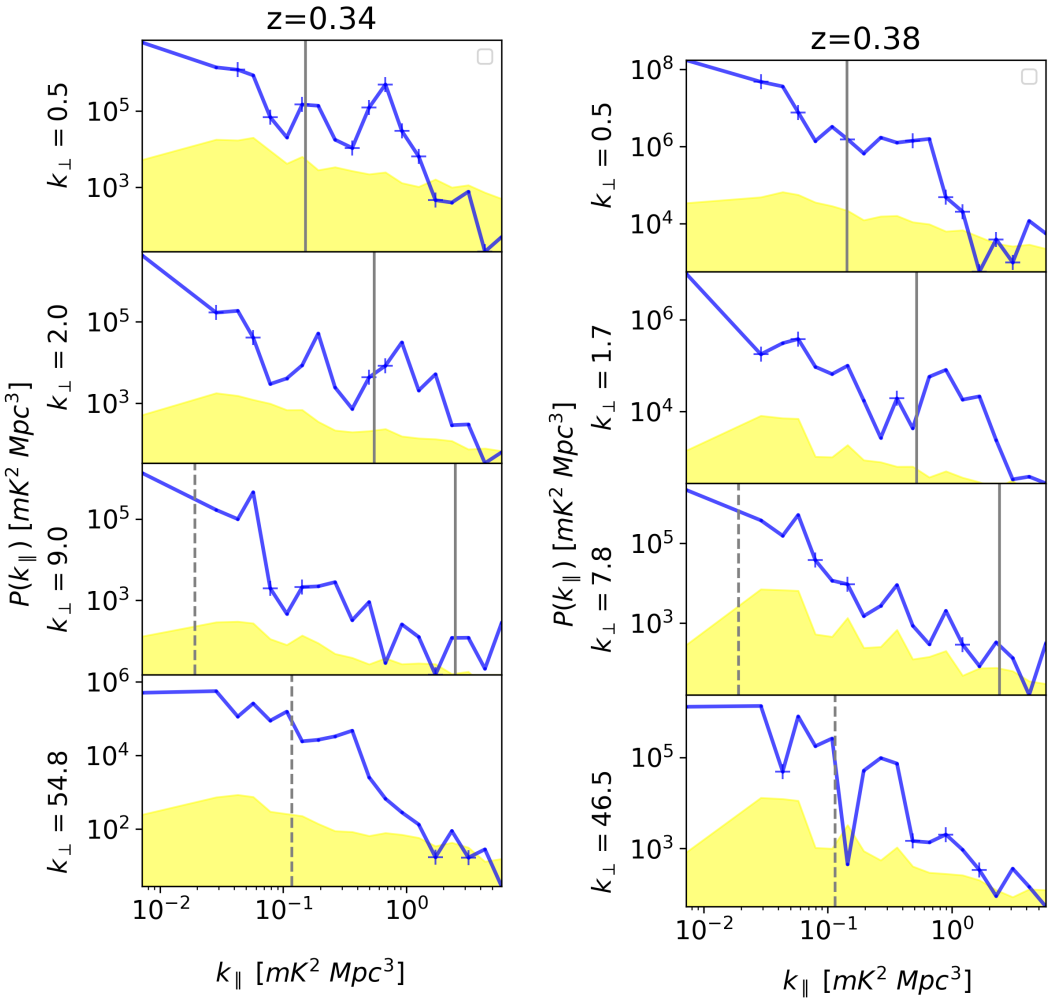

Figure 4.15: The absolute value of $P(k_\perp, k_\parallel)$ plotted against $k_\parallel$ at z=0.34 and z=0.38 for 4 $k_\perp$ values. The yellow shaded regions correspond to the 1σ errors due to system noise.

Figure 4.15 is a 1d profile showing $P(k_\perp, k_\parallel)$ against $k_\parallel$ at 4 different $k_\perp$ values. We see that the power decreases by several orders of magnitude from the smallest to largest $k_\parallel$ bin. Also, it appears that the noise limit is reached at high $k_\parallel$ values.

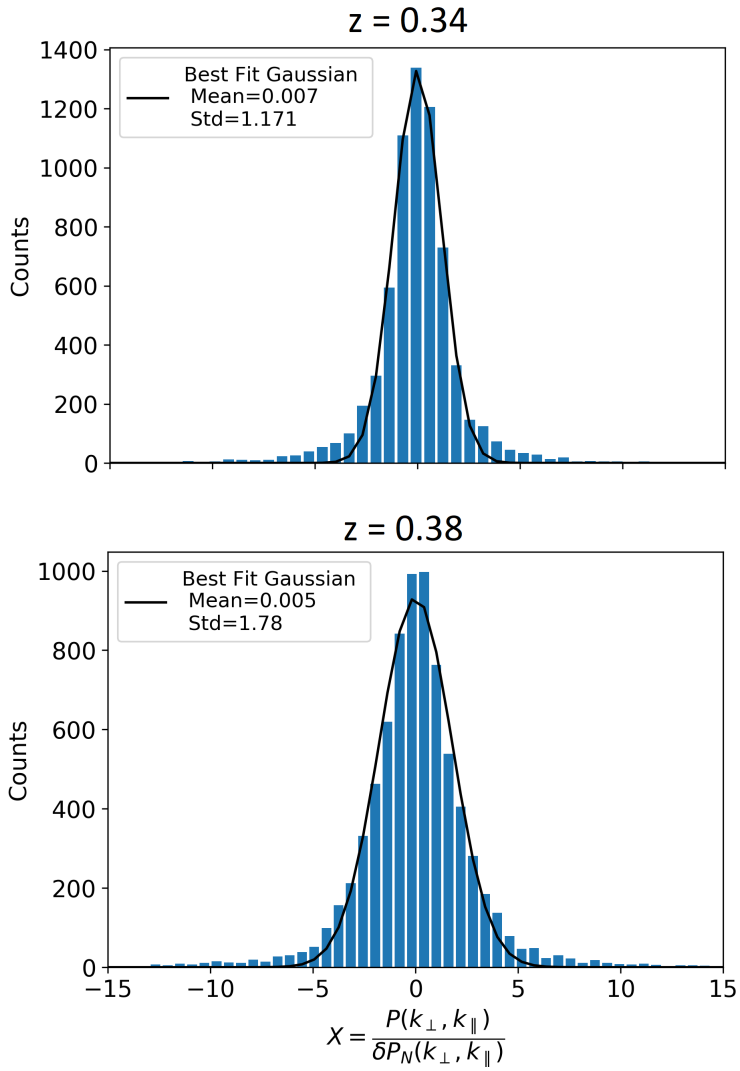

Figure 4.16: Histogram of X in the region away from foregrounds at z=0.34 and z=0.38.

Figure 4.16 is a plot of the histogram of variable X in the regions enclosed by the green lines in Figure 4.14. The best fit Gaussian gives $\mu(X) > 0$ and $\sigma(X) > 1$ for both z=0.34 and z=0.38. This indicates the presence of residual foregrounds in the region in k space that is used for obtaining the spherical power spectrum.

The spherical power spectrum P(k) in the whole k range and the window are plotted in Figure 4.17, with the dimensionless power spectra as insets. The error bars correspond to $2 \times \sigma(X) \times \delta P_N(k)$. We see a large decrease in the power values, by about 3 orders of magnitude, as we go to the region in k space relatively free of foregrounds.

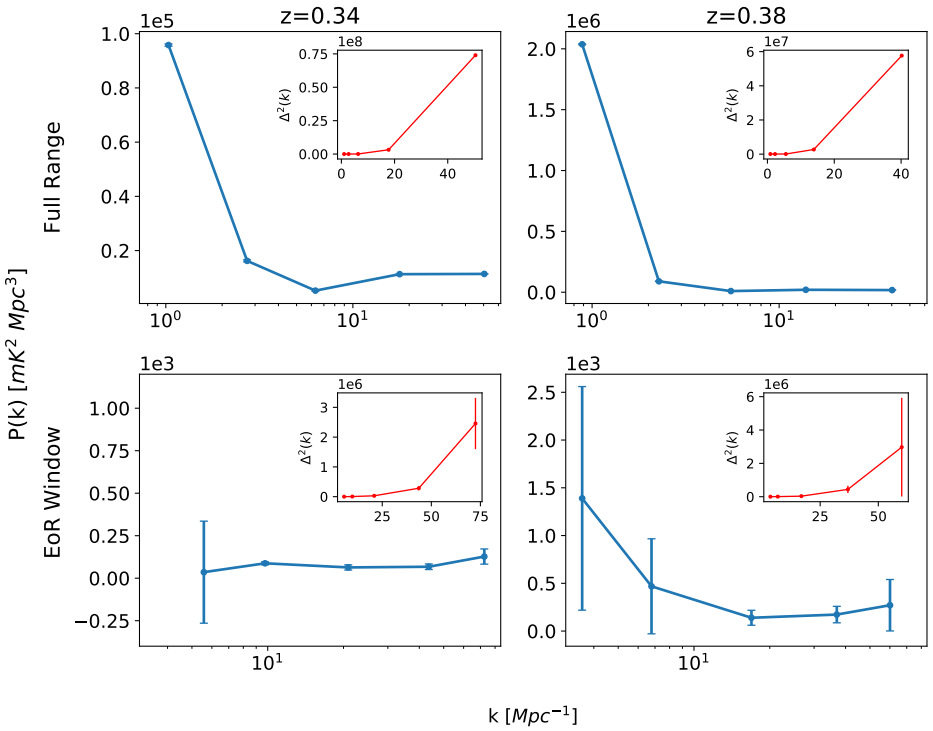

Figure 4.17: Spherical PS at z=0.34 and z=0.38. The top panel is when the values in the entire k range are used to compute the spherical PS. The bottom panel shows the results when only a region in the EoR window is used to bin the power values. Plots of $\Delta^2(k)$ against k are shown as insets in the corresponding panels.

4.3.2 Constraints on $\Delta^2(k)$ and $\Omega_{HI}b_{HI}$

The dimensionless power spectrum and the error bars are used to set the 2σ upper limits on $\Delta^2(k)$ at z=0.34 and z=0.38. The results are summarized in Table 4.4.

A comparison with the linear dark matter power spectrum yields upper limits on $\Omega_{HI}\times b_{HI}$ in a manner similar to what is described in 4.2.3. The results are summarized in Table 4.5.

Figure 4.18 shows the comparison of the 2σ upper limits at z=0.34 and z=0.38 with the predicted $\Delta^2_{HI}(k)$. We see that the estimated limits are more that 3 orders of magnitude higher than the predicted values.

k $[Mpc^{-1}]$	$\Delta^2(k)$ $[mK^2]$	σ $[mK^2]$	$\Delta^2_U(k)$ $[mK^2]$
5.56	$(17.63)^2$	$(36.30)^2$	$(54.28)^2$
9.76	$(64.22)^2$	$(14.24)^2$	$(67.30)^2$
20.88	$(171.05)^2$	$(59.52)^2$	$(190.64)^2$
43.64	$(532.39)^2$	$(185.56)^2$	$(593.55)^2$
72.50	$(1567.65)^2$	$(656.52)^2$	$(1821.97)^2$

k $[Mpc^{-1}]$	$\Delta^2(k)$ $[mK^2]$	σ $[mK^2]$	$\Delta^2_U(k)$ $[mK^2]$
3.60	$(57.21)^2$	$(30.11)^2$	$(71.32)^2$
6.78	$(86.03)^2$	$(50.84)^2$	$(112.12)^2$
16.92	$(184.79)^2$	$(79.47)^2$	$(216.28)^2$
36.92	$(663.58)^2$	$(269.00)^2$	$(764.89)^2$
60.07	$(1723.73)^2$	$(986.43)^2$	$(2217.51)^2$

Table 4.4: Upper limits on the dimensionless power spectrum at z = 0.34 (top) and z=0.38 (bottom).

k $[Mpc^{-1}]$	5.56	9.76	20.88	43.64	72.5
$\Omega_{HI} \times b_{HI}$ $[10^{-2}]$	6.02	6.64	16.39	45.45	129.95

k $[Mpc^{-1}]$	3.60	6.78	16.92	36.92	60.07
$\Omega_{HI} \times b_{HI}$ $[10^{-2}]$	8.61	11.72	18.97	59.08	159.65

Table 4.5: Upper limits on the the quantity $\Omega_{HI} \times b_{HI}$ at z = 0.34 (top) and z=0.38 (bottom).

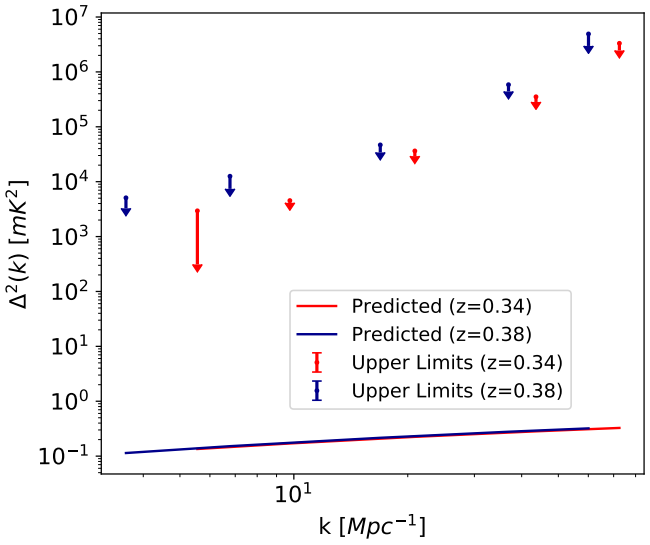

Figure 4.18: The estimated $\Delta^2_U(k)$ and predicted $\Delta^2_{HI}(k)$ at z=0.34 and z=0.38.

4.4 Summary

We have used the Tapered Gridded Estimator to estimate the power spectrum of brightness temperature fluctuations using observations of EGS made using the GMRT. The GSB data is at a redshift of 0.028 while the GWB datasets are at redshifts of 0.34 and 0.38. Following is a brief summary of the analysis of the GSB data.

- The TGE is applied to individual night observations separately. The estimated MAPS and PS across the different nights are fairly consistent and show the expected behaviour with tapering.
- All point sources above a flux threshold of 7σ are modelled and subtracted from the visibilities. The TGE is applied to the entire observation data before and after point source subtraction, with tapering fractions of f=3 and f=0.8. The effect of tapering and point source subtraction on the estimated MAPS and PS is studied.
- The oscillations seen in the plots of $C_\ell(\Delta\nu)$ against $\Delta\nu$ at large ℓ are attributed to residual point sources between the horizon and the null. Point source subtraction decreases the magnitude of the estimated MAPS only at large ℓ.
- The cylindrical power spectrum is seen to have values differing by 7 orders of magnitude from the smallest to the larges $k_\parallel$ bins. The high values at low $k_\parallel$ is due to foregrounds. Both tapering and point source subtraction suppress the effect of these foregrounds. To avoid the foregrounds and the effect of convolution, a region in the k space is chosen for obtaining the spherical power spectrum and the distribution of the quantity X = $\frac{P(k_\perp,k_\parallel)}{\delta P_N(k_\perp,k_\parallel)}$.
- The histogram of the quantity X is used to compare the observed distribution of errors with the distribution of errors expected due to system noise. $\mu(X) > 0$ and $\sigma(X) > 1$ indicates the presence of residual foregrounds which decrease after point source subtraction.
- The Spherical power spectrum and the dimensionless power spectrum are obtained. The power spectrum for f=0.8, after point source subtraction and in the region free of foregrounds, is used to set the upper limits for $\Delta^2(k)$ at the five smallest k bins. The simulated dark matter power spectrum at this

redshift is then used to estimate upper limits on $\Omega_{HI}b_{HI}$. The tightest constraints are obtained at k = 20.73 Mpc^{-1} and the estimated 2σ upper limits are: $\Delta^2(k) = (17.14)^2 mK^2$ and $\Omega_{HI}b_{HI} = 0.0179$.

- However, these limits are not of much physical interest since the scales probed are very small and the total comoving volume probed is also not representative. This suggests the need to repeat the analysis at higher redshift (to probe larger volumes) and with a larger bandwidth (to gain access to smaller $k_{\parallel}$ modes). Therefore, we have repeated this analysis on two small sections of the GWB data at z=0.34 and z=0.38.

Following is a brief summary of the GWB data analysis and results obtained:

- The MAPS exhibit oscillations which can be attributed to sources of foreground located between the first null and horizon.
- The Cylindrical PS shows a clear foreground wedge at high $k_{\perp}$ at both z=0.34 and z=0.38. Regions in k space outside the foreground wedge are used to obtain the binned spherical power spectrum.
- The variable X exhibits $\mu(X) > 0$ and $\sigma(X) > 1$ at both z=0.34 and z=0.38.
- The tightest constraints are obtained at k=$5.56 Mpc^{-1}$ for z=0.34. The 2σ upper limits are $\Delta^2_U(k) = (54.28)^2 mK^2$ and $\Omega_{HI}b_{HI} = 6.02 \times 10^{-2}$. For z=0.38, the tightest constraints are at k=$3.60 Mpc^{-1}$. The 2σ upper limits are $\Delta^2_U(k) = (71.32)^2 mK^2$ and $\Omega_{HI}b_{HI} = 8.61 \times 10^{-2}$.

Bibliography

[Anderson 18] CJ Anderson, NJ Luciw, Y-C Li, CY Kuo, J Yadav, KW Masui, TC Chang, X Chen, N Oppermann, YW Liao*et al. Low-amplitude clustering in low-redshift 21-cm intensity maps cross-correlated with 2dF galaxy densities.* Monthly Notices of the Royal Astronomical Society, vol. 476, no. 3, pages 3382–3392, 2018.

[Bagla 97] Jasjeet Singh Bagla & T Padmanabhan. *Cosmological N-body simulations.* Pramana, vol. 49, no. 2, pages 161–192, 1997.

[Bera 19] Apurba Bera, Nissim Kanekar, Jayaram N Chengalur & Jasjeet S Bagla. *Atomic hydrogen in star-forming galaxies at intermediate redshifts.* The Astrophysical Journal Letters, vol. 882, no. 1, page L7, 2019.

[Bharadwaj 05] Somnath Bharadwaj & Sk Saiyad Ali. *On using visibility correlations to probe the Hi distribution from the dark ages to the present epoch–I. Formalism and the expected signal.* Monthly Notices of the Royal Astronomical Society, vol. 356, no. 4, pages 1519–1528, 2005.

[Bharadwaj 19] Somnath Bharadwaj, Srijita Pal, Samir Choudhuri & Prasun Dutta. *A Tapered Gridded Estimator (TGE) for the multifrequency angular power spectrum (MAPS) and the cosmological H i 21-cm power spectrum.* Monthly Notices of the Royal Astronomical Society, vol. 483, no. 4, pages 5694–5700, 2019.

[Bobin 16] J Bobin, F Sureau & J-L Starck. *Cosmic microwave background reconstruction from WMAP and Planck PR2 data.* Astronomy & Astrophysics, vol. 591, page A50, 2016.

[Bonaldi 15] Anna Bonaldi & Michael L Brown. *Foreground removal for Square Kilometre Array observations of the epoch of reionization with the*

correlated component analysis. Monthly Notices of the Royal Astronomical Society, vol. 447, no. 2, pages 1973–1983, 2015.

[Chapman 12] Emma Chapman, Filipe B Abdalla, Geraint Harker, Vibor Jelić, Panagiotis Labropoulos, Saleem Zaroubi, Michiel A Brentjens, AG de Bruyn & LVE Koopmans. *Foreground removal using FASTICA: a showcase of LOFAR-EoR*. Monthly Notices of the Royal Astronomical Society, vol. 423, no. 3, pages 2518–2532, 2012.

[Choudhuri 14] Samir Choudhuri, Somnath Bharadwaj, Abhik Ghosh & Sk Saiyad Ali. *Visibility-based angular power spectrum estimation in low-frequency radio interferometric observations*. Monthly Notices of the Royal Astronomical Society, vol. 445, no. 4, pages 4351–4365, 2014.

[Choudhuri 16] Samir Choudhuri, Somnath Bharadwaj, Suman Chatterjee, Sk Saiyad Ali, Nirupam Roy & Abhik Ghosh. *The visibility-based tapered gridded estimator (TGE) for the redshifted 21-cm power spectrum*. Monthly Notices of the Royal Astronomical Society, vol. 463, no. 4, pages 4093–4107, 2016.

[Datta 07] Kanan K Datta, T Roy Choudhury & Somnath Bharadwaj. *The multifrequency angular power spectrum of the epoch of reionization 21-cm signal*. Monthly Notices of the Royal Astronomical Society, vol. 378, no. 1, pages 119–128, 2007.

[Ewen 51] Harold Irving Ewen & Edward Mills Purcell. *Observation of a line in the galactic radio spectrum*. In Classics in Radio Astronomy, pages 328–330. Springer, 1951.

[Ghosh 12] Abhik Ghosh, Jayanti Prasad, Somnath Bharadwaj, Sk Saiyad Ali & Jayaram N Chengalur. *Characterizing foreground for redshifted 21 cm radiation: 150 MHz Giant Metrewave Radio Telescope observations*. Monthly Notices of the Royal Astronomical Society, vol. 426, no. 4, pages 3295–3314, 2012.

[Hand 18] Nick Hand, Yu Feng, Florian Beutler, Yin Li, Chirag Modi, Uroš Seljak & Zachary Slepian. *nbodykit: An open-source, massively parallel toolkit for large-scale structure*. The Astronomical Journal, vol. 156, no. 4, page 160, 2018.

[Jansky 33] Karl G Jansky. *Electrical disturbances apparently of extraterrestrial origin.* Proceedings of the Institute of Radio Engineers, vol. 21, no. 10, pages 1387–1398, 1933.

[Jones 18] Michael G Jones, Martha P Haynes, Riccardo Giovanelli & Crystal Moorman. *The ALFALFA H i mass function: a dichotomy in the low-mass slope and a locally suppressed 'knee'mass.* Monthly Notices of the Royal Astronomical Society, vol. 477, no. 1, pages 2–17, 2018.

[Liu 20] Adrian Liu & J Richard Shaw. *Data Analysis for Precision 21 cm Cosmology.* Publications of the Astronomical Society of the Pacific, vol. 132, no. 1012, page 062001, 2020.

[Mertens 18] FG Mertens, A Ghosh & LVE Koopmans. *Statistical 21-cm signal separation via Gaussian Process Regression analysis.* Monthly Notices of the Royal Astronomical Society, vol. 478, no. 3, pages 3640–3652, 2018.

[Mertens 20] Florent G Mertens, M Mevius, Leon VE Koopmans, AR Offringa, Garrelt Mellema, Saleem Zaroubi, MA Brentjens, H Gan, Bharat Kumar Gehlot, VN Pandey*et al. Improved upper limits on the 21 cm signal power spectrum of neutral hydrogen at z≈ 9.1 from LOFAR.* Monthly Notices of the Royal Astronomical Society, vol. 493, no. 2, pages 1662–1685, 2020.

[Mitchell 08] Daniel A Mitchell, Lincoln J Greenhill, Randall B Wayth, Robert J Sault, Colin J Lonsdale, Roger J Cappallo, Miguel F Morales & Stephen M Ord. *Real-time calibration of the Murchison Widefield Array.* IEEE Journal of Selected Topics in Signal Processing, vol. 2, no. 5, pages 707–717, 2008.

[Pal 21] Srijita Pal, Somnath Bharadwaj, Abhik Ghosh & Samir Choudhuri. *Demonstrating the Tapered Gridded Estimator (TGE) for the cosmological H i 21-cm power spectrum using 150-MHz GMRT observations.* Monthly Notices of the Royal Astronomical Society, vol. 501, no. 3, pages 3378–3391, 2021.

[Parsons 09] Aaron R Parsons & Donald C Backer. *Calibration of low-frequency, wide-field radio interferometers using delay/delay-rate filtering.* The Astronomical Journal, vol. 138, no. 1, page 219, 2009.

[Penzias 65] Arno A Penzias & Robert Woodrow Wilson. *A measurement of excess antenna temperature at 4080 Mc/s.* The Astrophysical Journal, vol. 142, pages 419–421, 1965.

[Platania 03] Paola Platania, C Burigana, D Maino, E Caserini, M Bersanelli, B Cappellini & A Mennella. *Full sky study of diffuse Galactic emission at decimeter wavelenghts.* Astronomy & Astrophysics, vol. 410, no. 3, pages 847–863, 2003.

[Pritchard 12] Jonathan R Pritchard & Abraham Loeb. *21 cm cosmology in the 21st century.* Reports on Progress in Physics, vol. 75, no. 8, page 086901, 2012.

[Sullivan 12] Ian S Sullivan, Miguel F Morales, Bryna J Hazelton, Wayne Arcus, David Barnes, Gianni Bernardi, Frank H Briggs, Judd D Bowman, John D Bunton, Roger J Cappallo*et al. Fast holographic deconvolution: A new technique for precision radio interferometry.* The Astrophysical Journal, vol. 759, no. 1, page 17, 2012.

[Swarup 91] Govind Swarup, S Ananthakrishnan, VK Kapahi, AP Rao, CR Subrahmanya & VK Kulkarni. *The giant metre-wave radio telescope.* Current science, vol. 60, no. 2, pages 95–105, 1991.